



**CHALMERS**  
UNIVERSITY OF TECHNOLOGY

---



# Connecting the Onsala Telescope Cluster Using Local Interferometry

Master's thesis in Wireless, Photonics and Space Engineering

VICTOR MARKNÄS



MASTER'S THESIS 2019

# Connecting the Onsala Telescope Cluster Using Local Interferometry

Victor Marknäs



Department of Space, Earth and Environment  
*Onsala Space Observatory*  
CHALMERS UNIVERSITY OF TECHNOLOGY  
Gothenburg, Sweden 2019

Connecting the Onsala Telescope Cluster using Local Interferometry  
Victor Marknäs

© VICTOR MARKNÄS, 2019.

Supervisor: Rüdiger Haas, Space, Earth and Environment, Chalmers University of technology

Examiner: Rüdiger Haas, Space, Earth and Environment, Chalmers University of technology

Master's Thesis 2019  
Department of Space Earth and Environment  
Onsala Space Observatory  
Chalmers University of Technology  
SE-412 96 Gothenburg  
Telephone +46 31 772 1000

Cover: The twin telescopes in the foreground, and the old 25 metre telescope in the background, at dusk

Typeset in L<sup>A</sup>T<sub>E</sub>X  
Gothenburg, Sweden 2019



Connecting the Onsala Twin Telescopes  
VICTOR MARKNÄS  
Department of Space, Earth and Environment  
Chalmers University of Technology

## Abstract

The transition from legacy  $S/X$  geodetic VLBI systems to dedicated broadband receivers represented by the VGOS system require a period of operational overlap between the new and the old systems. In order to do so, local-tie measurements between the co-located telescopes at OSO and other sites needs to be performed to place the telescopes in the same reference frame. A working methodology and performance analysis of such measurements has been performed at the Onsala Space Observatory, and show promising results for future work, both locally and globally. With these results, transition to a fully operational VGOS system will be made possible.

Keywords: VLBI, VGOS, local tie-vectors, correlation, geodesy.



# Acknowledgements

First of all, I would like to thank my supervisor, Rüdiger Haas for his support during this thesis work. Without your knowledge, skill and patience over these last few months, this would have never gone the way it did. It's been a pleasure and extremely educational to be allowed to work with your telescopes at the observatory. I would also like to extend thanks to the guys in the GEO group for your invaluable help in running software and analysis, as well as your knowledge, and to the many people at the observatory I've had the pleasure of meeting during these months. Our vivid and far-reaching discussions about nothing in particular during lunches and bus-rides to and from the observatory kept me sane during this process.

I also extend my thanks to the madlads that I've gotten to know since the start of my education here at Chalmers. Our collective nervous breakdowns over the years still resonate in my memory. Without you guys, these years would have been a lot worse.

Last, but not least, my dearest Eva. Without your unwavering support and faith in my ability, I would have surrendered many years ago.

*Per aspera, ad astra*

Victor Marknäs, Gothenburg, September 23, 2019



# Contents

<b>List of Figures</b>	<b>xi</b>
<b>List of Tables</b>	<b>xiii</b>
<b>1 Introduction</b>	<b>1</b>
1.1 Background . . . . .	1
1.2 Aim . . . . .	2
1.3 Demarcations . . . . .	2
1.4 Ethical, Societal and Environmental Considerations . . . . .	3
<b>2 Theory</b>	<b>5</b>
2.1 Geodetic Very Long Baseline Interferometry . . . . .	5
2.2 The Correlator Output . . . . .	8
2.3 Bandwidth Synthesis . . . . .	9
2.4 Reference Systems and Frames . . . . .	10
2.4.1 The Celestial Reference Frame . . . . .	11
2.4.1.1 Celestial Coordinates . . . . .	11
2.4.2 The Terrestrial Reference Frame . . . . .	13
2.5 Timekeeping in a VLBI Context . . . . .	13
2.6 Correlator Operations . . . . .	13
2.6.1 Correlator Architectures . . . . .	14
2.6.1.1 Antenna Based Operations . . . . .	14
2.6.1.2 Baseline-based Operations . . . . .	15
2.7 Post-correlator Operations - Fringe Fitting . . . . .	15
2.8 Parameter Estimation in $\nu$ Solve . . . . .	16
<b>3 Methods</b>	<b>17</b>
3.1 Baseline Measurements Between the two Twin Telescopes . . . . .	18
3.2 Baseline Measurements Between the OTT and the 20 Metre Telescope	18
3.2.1 New Firmware on the Digital Baseband Converter (DBBC) . .	19
3.3 Data Recording and Processing Workflow . . . . .	20
3.3.1 Recording . . . . .	20
3.3.2 Processing . . . . .	20
3.4 Phase Corrections . . . . .	21
3.4.1 Phase Stability . . . . .	22
3.4.2 Manual Phase Calibration . . . . .	22
3.4.3 Polarization Products . . . . .	24

3.5	Tropospheric Corrections . . . . .	25
3.6	Scheduling of Observations . . . . .	26
3.7	Extended Bandwidth Using all Available Channels . . . . .	26
<b>4</b>	<b>Results</b>	<b>27</b>
4.1	Early Experimentation . . . . .	27
4.2	Experiments on the Onsala Telescope Cluster . . . . .	29
4.2.1	K9092 . . . . .	31
4.3	Results of Pressure Adjustment . . . . .	33
4.3.1	No Pressure Correction . . . . .	33
4.3.2	With Pressure Correction . . . . .	34
4.4	Summary of results . . . . .	35
4.4.1	Shorter Data Segments and Multiband Solutions . . . . .	36
4.5	24 hour sessions - Multiband and Phase Solutions . . . . .	37
<b>5</b>	<b>Conclusion</b>	<b>39</b>
5.1	Analysis and Discussion on the Results . . . . .	39
5.1.1	A note on the Omitted Frequency Channel . . . . .	39
5.2	Future Work . . . . .	40
	<b>Bibliography</b>	<b>41</b>
<b>A</b>	<b>Appendix 1 - Example *.vex and *.v2d files</b>	<b>I</b>
A.1	Example *.vex file . . . . .	I
A.2	Example *.v2d file . . . . .	V
<b>B</b>	<b>Appendix 2 - Scripts</b>	<b>VII</b>
B.1	fieldReplacer . . . . .	VII
B.2	vex2refsource . . . . .	VIII

# List of Figures

2.1	Basic two-dimensional schematic of an interferometer geometry . . . .	6
2.2	An example of a VLBI fringe, taken from an experiment performed on 30th of April. The blue graph shows the multiband delay from 8 frequency channels, while the red graph shows the <i>delay rate</i> or time derivative of the delay. . . . .	9
2.3	Figure showing the geometry required to determine the position of a celestial object based on its right ascension and declination. The horizon refers to the local horizon of the observer. . . . .	12
3.1	Overhead screenshot from <i>Google Maps</i> of the telescopes and baselines utilized in the course of this thesis work. . . . .	18
3.2	Example of a recorded X-band Channel and the different bandwidths of the different telescopes. The narrower red box corresponds to the On telescope and the broader red box corresponds to the OTT. The height of the boxes are irrelevant and only for clarity. . . . .	19
3.3	Block diagram of correlator workflow showing what files are being generated and used in what instance. <i>Italics</i> show file endings, and regular block letters show file types. . . . .	21
3.4	Correlated phase calibration tones in the X-band on the LW baseline	22
3.5	Comparison of fringe detections using manual phase calibration. These are <i>fourfit</i> plots cropped and edited to highlight the corrected phases, and to display differences in fringe quality and SNR. The phase offset $\Delta\phi$ (red line in lower parts of each graph) is clearly seen in the lowermost two pictures . . . . .	24
4.1	Fringe plots from experiments K9092c and K19120 showing a clear difference between a "bad" (upper figure) setup and a "good" (lower figure) one. . . . .	28
4.2	Multiband delay residuals on the OTT baseline from an entire 24 hour session. The delay residuals are on the order of 20-40 ps corresponding to a WRMS of 2.07 mm. . . . .	30
4.3	Multiband delay residuals on the OE-ON baseline from an entire 24 hour session. The delay residuals are on the order of 20-50 ps corresponding to a WRMS of 6.15 mm. . . . .	30
4.4	Multiband delay residuals on the OW-ON baseline from an entire 24 hour session. The delay residuals are on the order of 20-50 ps corresponding to a WRMS of 6.09 mm. . . . .	31

4.5	Fringe plot output from <i>fourfit</i> , showing fringes between On and Oe. The residual single and multiband delays are shown together with the fringe rate in the middle left and top windows respectively. The averaged power spectrum of the eight channels along with the averaged measured phase is shown in the middle right, and lastly the individual channel amplitudes and phases are shown as a time series in the bottom window. . . . .	32
4.6	The WRMS of all experiments, with no correction made for air pressure	33
4.7	Plots of scatter around the average baseline length, calculated from all included sessions. Scatter in mm along the y-axis and session name on the x-axis. The dashed lines represent the maximum and minimum scatter, respectively. . . . .	34
4.8	The WRMS of all experiments, with corrections made for air pressure	34
4.9	Plots of scatter around the average baseline length, calculated from all included sessions. Scatter in mm along the y-axis and session name on the x-axis. The dashed lines represent the maximum and minimum scatter, respectively. . . . .	35
4.10	Plots of scatter around the average baseline length, calculated from all included sessions. Scatter in mm along the y-axis and session name on the x-axis. The dashed lines represent the maximum and minimum scatter, respectively. . . . .	37
4.11	Comparison of delay residuals from Multiband (upper figure) and Phase (lower figure) evaluation. This figure shows the result on the OTT baseline. The scale of the Multiband residuals is $\pm 0.1$ ns, while the scale of the Phase residuals is $\pm 0.01$ ns . . . . .	38



# List of Tables

3.1	Eight-channel frequency setup used for the experiments performed in this master's thesis . . . . .	19
3.2	Difference of phases in degrees between frequency channels for some high-SNR scans in experiment <i>K19120</i> . . . . .	22
3.3	Estimated air pressure difference at the Onsala Telescopes. $\Delta P$ of the telescopes compared to the pressure gauge . . . . .	25
4.1	Results from <i><math>\nu</math>solve</i> for experiment K9092a . . . . .	32
4.2	WRMS of baseline residuals for each evaluated session in mm, together with the baseline lengths in metres, with uncertainty in mm. No additional pressure correction in log files for <i><math>\nu</math>Solve</i> . . . . .	33
4.3	WRMS of baseline residuals for each evaluated session in mm, together with the baseline lengths in metres, with uncertainty in mm. With pressure correction in log files . . . . .	35
4.4	Details on the Experiments Used in this Analysis . . . . .	36
4.5	WRMS of baseline residuals for each evaluated session in mm, together with the baseline lengths in metres, with uncertainty in mm. All available sessions, with pressure correction performed as outlined above. . . . .	36
4.6	WRMS of baseline residuals for each evaluated session in mm, together with the baseline lengths in metres, with uncertainty in mm. Solution based on 24 hour data sets solving for both multiband and phase delays. . . . .	37



# 1

## Introduction

The purpose of this section is to introduce the problem this thesis work intends to solve, as well as placing the work within a larger context. Some limitations on the scope of the work will also be described here.

### 1.1 Background

In 2017, two new telescopes were inaugurated at the Onsala Space Observatory. They are referred to as the Onsala Twin Telescopes (OTT), and are purpose-built for the Very Long Baseline Interferometry (VLBI) Global Observing System (VGOS) intended to work as a pair to contribute to the International VLBI service for Geodesy and Astrometry (IVS). One of the principal ideas behind the VGOS system (VLBI2010) is to utilize dedicated stations for geodetic VLBI, instead of "piggybacking" on older telescopes as has historically been the case. Not only will this allow for more consistent data with a higher throughput closer to real-time, but it also frees up the older telescopes to again focus on radio astronomy. The Onsala observatory currently operates a pair of older telescopes that among other things are used for geodetic VLBI using the legacy  $S/X$  (referring to the frequency bands used) system, together with the newer VGOS system represented by the twin telescopes. To maintain consistency and quality of the data series and geodetic reference frames, the legacy telescopes need to be connected to the newer VGOS telescopes on an observational level. In order to do so, local-tie measurements using short baseline interferometry between the telescopes at the Onsala Space Observatory will be utilized.

The structure of this text is as follows; The first chapter introduces and contextualizes the topic at hand, while the second chapter introduces the reader to the fundamental theories needed to understand the principles of radio interferometry in the context of geodetic VLBI with a basis in signal reception and processing. The third chapter describes the methodology used and familiarize the reader with the tools used in the pursuit of accurate position determination. The fourth will showcase the results and the fifth and final chapter consists of a discussion of the results, a conclusion and a look into future work needed.

Due to the limitation in scope of a master's thesis, it is assumed that the reader has some working knowledge of signal processing, signal reception and receiver design. These topics will only be covered briefly when necessary, and the topics particular to the task at hand will be expanded upon and placed in the context of geodetic VLBI.

### 1.2 Aim

The goal of this thesis work is to provide a working methodology to determine the relative position of the telescopes at the observatory. Because the older 20 metre telescope and the newer Twin Telescopes operate at different frequency bands and polarizations (right hand circular in the case of the 20 metre, horizontal and vertical linear polarization in the case of the OTT), observational strategies to account for these differences must be developed and validated. Due to the nature of geodetic VLBI measurements and the fact that the telescopes at Onsala are currently in use for experiments not strictly related to this thesis, a less than optimal number of measurements might have to be performed to avoid scheduling conflicts. If so, the observations made will be used as proof-of-concept and a basis for future work.

### 1.3 Demarcations

This thesis will assume that the reader is somewhat familiar with common signal reception and processing concepts such as frequency downconversion, sampling and correlation. Where necessary, such concepts will be described briefly, and placed into the context of the thesis work itself. Application-specific concepts particular to interferometry in general, and geodetic VLBI in particular will be given due attention to familiarize the reader with these concepts as they relate to the observation and their results. This thesis work will not address characterization of the antenna and receiver systems in terms of their performance, as much of this work is already done [1]. Where appropriate, using previous work, relevant performance parameters will be defined and described.

Further, this project will to a large extent utilize already established software for scheduling of observations, signal processing and data analysis, modified where necessary. New software will not be developed, as this in and of itself is beyond the scope of a master's thesis.

Even though the OTT will be part of a larger global network, only local interferometry will be performed to establish tie-vectors between the telescopes of the Onsala cluster. In principle, utilizing observations from telescopes at other observatories around the world, could be performed, but the increased complexity in signal processing, tropospheric corrections among other things, along with the potential difficulties in arranging schedules, as well as the data requiring transfer to the Onsala correlator for analysis, puts this out of the scope of a master's thesis. As such, this work will be performed using the 20 metre telescope and the twin telescopes.

### A note on the Operational Status of the Onsala Twin Telescopes

During the course of this thesis work, a number of issues plaguing the control and pointing systems of the twin telescopes presented themselves, limiting the available telescope time for co-location of the telescopes at the observatory. These issues are beyond the scope of this thesis to address and correct, but it should at least be men-

tioned in order to at least partly explain the relatively low amount of experiments performed. Due to these issues, the twin telescopes were at times out of commission for weeks at a time, and together with the scheduled VGOS experiments, the allotted time on the telescopes for this thesis was severely limited. These issues have since then been resolved.

## **1.4 Ethical, Societal and Environmental Considerations**

### **Societal**

With GNSS systems for personal use being extremely widespread in the form of hand-held receivers such as cellular phones, and an existing push towards self-driving cars, there is a justification in maintaining and further developing the reference frames used for among other things accurate positioning. This can only be done if new technologies and approaches are developed and used.

Accurate modelling of the reference frames also paves the way for a deeper understanding of the universe and the planet's place in it. This is clearly a boon to astronomers worldwide, but humanity as a whole stands to gain from a greater understanding of the cosmos around us.

### **Environmental**

The establishment of accurate celestial and terrestrial reference frames allows for a more precise modelling of the planet and its dynamics. The existence of an accurate reference frame is one of many factors critical for environmental modelling, allowing for better weather and climate predictions. A direct application of VLBI that exists today is modelling of the troposphere, applicable both to GNSS measurements and atmospheric modelling [2]. The United Nations has also declared the necessity of a global cooperation, as opposed to national services, for the maintenance and development of accurate reference frames [3].



# 2

## Theory

In the following section, the theory needed to understand the concept of interferometry in general and VLBI in particular is introduced and developed. The specific theories regarding geodetic VLBI will also be introduced here to give the reader a solid theoretical footing for the method and results chapters. This text will not delve into the details of radio interferometry in terms of imaging capability, resolution, or sensitivity enough to detect a black hole [4] and other finer points of interferometry. Instead, focus will be on the concepts central to geodetic VLBI. For a more in-depth perspective on radio interferometry, refer to available literature instead. Used heavily in this report are among others *Interferometry and Synthesis in Radio Astronomy* (Thompson et al.) [5] and *VLBI - A fascinating technique for geodesy and astrometry* (Schuh & Behrend). [6]

### 2.1 Geodetic Very Long Baseline Interferometry

The underlying principle of geodetic VLBI is relatively simple; The fundamental observable is the measured time delay of a signal from an extragalactic source such as a quasar [6], received at two or more telescopes. For simplicity, this text will describe the principle of geodetic VLBI using two telescopes, but the principle remains the same when adding more telescopes, since all operations are performed on a per-baseline basis. The incoming radiation from a given source is amplified, downconverted and digitally sampled. At this point in time, it shall be noted that no observable exists. Instead, the desired quantity,  $\tau$  is given only when the recorded data from the telescopes is correlated. The procedure and methodology of correlation will be described later in this text. In order to maintain proper timing each stations' signal processing devices (amplifiers, mixers, samplers etc.) time, frequency and phase information is derived coherently from an on-site atomic frequency standard, usually in the form of a hydrogen maser. The basic observational geometry for a "snapshot" observation is shown in Fig. 2.1 below.

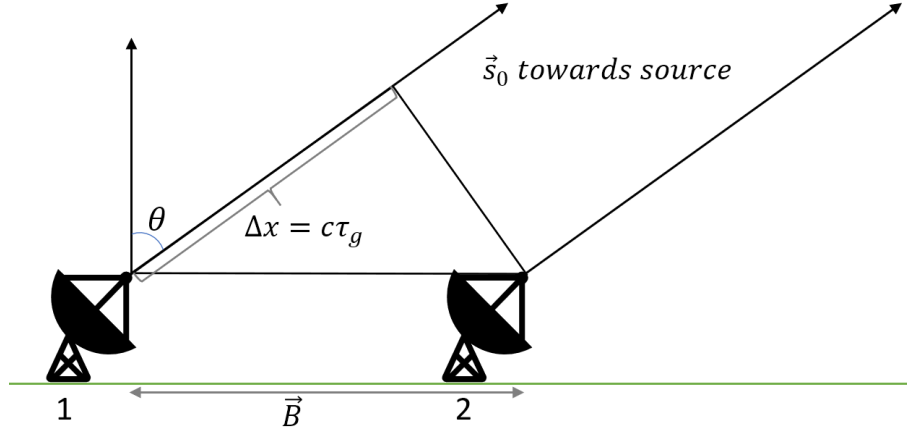


**Figure 2.1:** Basic two-dimensional schematic of an interferometer geometry

Because the sources used in geodetic VLBI tend to, and are preferred to be both point-like and very distant [7], the incoming radiation that reaches the antennas can be assumed to have a planar wavefront propagating along the unit vector,  $\vec{s}_0$ , to the source. When two telescopes separated by the baseline vector  $\vec{b}$  simultaneously point at the same source in the direction of  $\vec{s}_0$  and in the absence of other effects on the delay, the geometric delay  $\tau_g$  of the signal is determined by the scalar product of  $\vec{b}$  and  $\vec{s}_0$  divided by the speed of light,  $c$ , assuming no other disturbances from the atmosphere, earth rotation and so on.

$$\tau_g = -\frac{\vec{B} \cdot \vec{s}_0}{c} = -\frac{\vec{B}}{c} \sin \theta = t_1 - t_2 \quad (2.1)$$

Although the VLBI signal delay  $\tau$  measured at the correlator is dominated by the geometric delay,  $\tau_g$ , many other factors contribute to the measured quantity and must be taken into account for a highly accurate determination of the delay to be made. Adding correction terms yields the fundamental observation equation for VLBI [6]

$$\tau = \tau_g + \tau_{ab} + \tau_{clk} + \tau_{inst} + \tau_{trop} + \tau_{iono} + \tau_{rel}, \quad (2.2)$$

where  $\tau_g$  is the geometric delay, whereas  $\tau_{ab}$  is the contribution due to diurnal aberration (apparent motion of the source due to movement of receiver antennas),  $\tau_{clk}$  is the contribution to the delay caused by mis-synchronized reference clocks at each observatory and  $\tau_{inst}$  is the contribution from propagation delays through instruments or cables at the observatory. The latter two can be thought of as system-dependent errors which need to be calibrated. The atmosphere of the earth contributes the tropospheric delay  $\tau_{trop}$  and the ionospheric delay  $\tau_{iono}$ . Lastly are the relativistic corrections,  $\tau_{rel}$  to the classical geometric delay  $\tau_g$  [6]. Since the observations carried out within the framework of this thesis work will be performed on relatively short baselines (on the order of 500 metres), the delay caused by atmospheric refraction will be very similar as seen from either telescope due to a similar atmospheric column in the line of sight from either telescope. Because of this, the delay caused by atmospheric effects more or less cancels out in the correlation process. A major



disadvantage of the shorter baseline compared to the ones typically used in geodetic VLBI is that Radio-Frequency Interference (RFI) will be strongly correlated, which will be shown in later sections as well as by Schüller et al. in [8].

It shall also be noted that Eq. (2.1) as it is described here can be thought of as a "snapshot" of the time delay between the telescopes. In reality, longer experiments on the order of 30 seconds to several minutes are carried out in several hour intervals, and as such additional attention must be paid to the precession and nutation (or colloquially, "wobble") of the Earth, as well as the changing geometry of the observation.

Performing multiple measurements of  $\tau$  on multiple radio sources in sequence will result in a data set sufficient to overdetermine the baseline vector  $\vec{B}$  [6]. In order to find the delay, the bit streams from the two telescopes are cross-correlated, and the location of the peak in the cross-correlation function determines the total delay,  $\tau$ . As with any cross-correlation function, the width  $w$  of the central maxima of the the VLBI cross-correlation function is inversely proportional to the total bandwidth of the signals being cross-correlated. The precision with which the signal delay  $\tau$  can be determined is given by  $\sigma_\tau$  and is related to the total effective bandwidth,  $\nu_{RMS}$  of the correlated signal by [9], [7],

$$\sigma_\tau \propto \frac{1}{2\pi} \cdot \frac{1}{SNR \cdot \nu_{RMS}} = \frac{1}{2\pi} \cdot \frac{1}{SNR \sqrt{\langle (\nu_i - \bar{\nu})^2 \rangle}}, \quad (2.3a)$$

$$SNR \propto \frac{S\sqrt{N}}{\sqrt{SEFD_i \cdot SEFD_j}}, \quad (2.3b)$$

$$SEFD_i \propto \frac{T_{sys}}{\eta_A T_A}. \quad (2.3c)$$

The above relations require some clarification in order to proceed. Equation 2.3a gives a relation between signal-to-noise ratio, SNR, and the spanned bandwidth,  $\nu_{RMS}$ . The terms  $\nu_i$  and  $\bar{\nu}$  denote the center frequency of each channel in all bands and mean of center frequencies, respectively, whereas the  $\langle \rangle$  denotes averaging. The signal-to-noise ratio in Eq. (2.3b) is related to the signal strength or flux density of the source,  $S$ , often expressed in Janskys ( $1 \text{ Jy} = 10^{-26} \text{ Wm}^{-2}\text{Hz}^{-1}$ ), the total number of samples,  $N$  and the System Equivalent Flux Density, SEFD for antennas  $i$  and  $j$ , respectively. It shall be noted that the SNR in the case of interferometric observations relates to the correlated SNR, rather than the SNR for the individual telescopes. The quantity SEFD describes the total received flux density required to raise the system temperature,  $T_{sys}$ , by a factor of two and is a measure of the system sensitivity [9].

In the case of the experiments performed in this masters thesis, as will be elaborated upon later in Section 3.2, utilized 8 frequency channels in the X-band around 8 GHz for a total spanned bandwidth of 720 MHz. Using Eq. (2.3a) above, and assuming an SNR on the order of a hundred to a few hundreds, and the frequency values found in Table 3.1 as an example, gives a value of  $\nu_{RMS}$  on the order of hundreds of MHz makes little difference in this case), one could get a perception of the expected performance these measurements should provide. With these things in mind, the expected uncertainties are on the order of

$$\sigma_\tau \approx \frac{1}{2\pi} \frac{1}{100 * 10^8} = 30 \text{ ps} \quad (2.4)$$

This translates to a range uncertainty of  $\sigma_r \approx c \cdot 30 \text{ ps} = 9 \text{ mm}$ . This magnitude of uncertainty justifies the VGOS system with its larger spanned bandwidth between S- and X-band, as discussed in the opening of this chapter.

## 2.2 The Correlator Output

This section is intended to introduce the reader to the underlying principle of radio interferometry as it relates to geodetic VLBI. Many of the finer points of interferometry will not be dealt with here, but can be found in the reference material for those who are interested. The analysis will start with the monochromatic case and from there derive the necessary components for the case of a broader bandwidth.

At face value the underlying principle of interferometry is relatively straight-forward. Again, referring to Fig. 2.1, consider two telescopes separated by a distance  $\vec{B}$  pointing at some (sufficiently) distant source along  $\vec{s}$  in the direction of  $\theta$ . If it can be assumed that the source of interest is located far enough away from the two telescopes (i.e. in the *far field* of either antenna) as well as being unresolved (i.e. of an angular size much smaller than the main lobe as described above), which is the case for geodetic VLBI sources, the incoming electromagnetic wavefront can be assumed to be planar upon arrival at the telescopes. For a monochromatic signal with frequency  $\nu$ , disregarding any processes that can disturb the signal, and thus assuming that the signal that reaches the two telescopes is identical apart from a time delay, the two antennas receive the signals [5]

$$V_1 = V \cdot \sin 2\pi\nu t, \quad (2.5a)$$

$$V_2 = V \cdot \sin (2\pi\nu(t - \tau_g)), \quad (2.5b)$$

where the delay  $\tau_g$  is given by

$$\tau_g = \frac{\vec{B}}{c} \sin \theta. \quad (2.6)$$

The two signals from each telescope are then coherently summed, time-averaged and multiplied and the output is a quantity with dimensions  $V^2$ . The output from the correlator is proportional to

$$\begin{aligned} F &\propto 2 \sin (2\pi\nu t) \sin (2\pi\nu(t - \tau_g)) \\ &= 2 \sin^2(2\pi\nu t) \cos (2\pi\nu\tau_g) - 2 \sin (2\pi\nu t) \cos (2\pi\nu t) \sin (2\pi\nu\tau_g). \end{aligned} \quad (2.7)$$

For typical geodetic observations, the frequency  $\nu$  is on the order of GHz. As the Earth rotates, the direction to the source  $\theta$  varies at most with a rate on the order of  $\frac{d\theta}{dt} \propto 10^{-4} \text{ rads}^{-1}$ . For terrestrial baselines,  $D$  cannot be larger than the vicinity of  $10^7$  metres. Consequently, the variation of  $\nu\tau_g$  is typically several orders of magnitude smaller than  $\nu t$ . Further, if an averaging period  $T \gg \nu^{-1}$  is used, which is typically

the case, the average value of  $\sin^2(2\pi\nu t) = \frac{1}{2}$  and the average value of  $\cos(2\pi\nu t) = 0$  the output from the correlator is thus

$$F = \cos(2\pi\nu\tau_g) = \cos\left(2\pi\nu\frac{D}{c}\sin(\theta)\right) = \cos\left(\frac{2\pi\nu D}{\lambda}l\right), \quad (2.8)$$

where  $l = \sin(\theta)$ . The above function is known as the *fringe function* and is a function that slowly varies with  $\theta$  in a quasi-sinusoidal fashion. Now, if instead of the monochromatic case, a band of frequencies of width  $\Delta\nu$  centered on a frequency  $\nu_0$  with a uniform spectral density inside the band is considered, the fringe function as a function of  $\theta$  can be expressed as

$$\begin{aligned} F(l) &= \frac{1}{\Delta\nu} \int_{\Delta\nu-\nu_0}^{\Delta\nu+\nu_0} \cos\left(\frac{2\pi\nu D l}{c}\right) d\nu \\ &= \cos\left(\frac{2\pi D l \nu_0}{c}\right) \frac{\sin\left(\pi D l \Delta\nu / c\right)}{\pi D l \Delta\nu / c}. \end{aligned} \quad (2.9)$$

Thus, the envelope of the fringe function is in the form of a sinc function ( $\text{sinc}(x) \equiv \frac{\sin(x)}{x}$ ) that varies with  $\theta$ , again, in the absence of noise. A real example of this, albeit in the presence of various types of noise and not yet properly solved for is shown in Fig. 2.2.

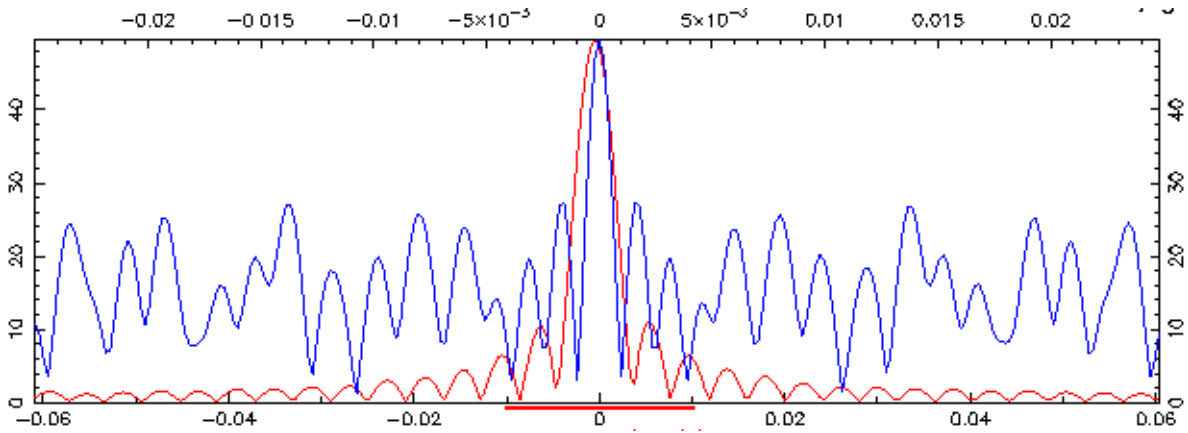


**Figure 2.2:** An example of a VLBI fringe, taken from an experiment performed on 30th of April. The blue graph shows the multiband delay from 8 frequency channels, while the red graph shows the *delay rate* or time derivative of the delay.

## 2.3 Bandwidth Synthesis

As mentioned previously in this chapter, one of the key parameters to accurate time delay measurements is the total bandwidth of the recorded signal. Theoretically, performing measurements with an extremely broad passband would allow for the required accuracy. However, due primarily to limitations in recording hardware, the bandwidth of any one signal recorded can not be arbitrarily large. Instead, a larger bandwidth can be synthesized by combining a set of narrower frequency channels

spread out over the band. This method is known as *bandwidth synthesis* (BWS) and is commonly used in VLBI observations due to its potential for allowing for a large bandwidth and thus high accuracy, while keeping the demands of individual recording channels lower [10],[11].

The relative time delay between the two antennas in an interferometer baseline is determined by sampling the delay resolution function (DRF) of the signals impinging on the two antennas as a function of time delay until a central maxima is found. The precision with which this function can be sampled is dependent on the width of the delay function's central maxima, whereas the width of the DRF is inversely proportional to the bandwidth of the observation. The confidence level of the detection is determined by the "risk" of confusing the secondary maxima (the highest sidelobe) with the central maxima of the delay function. The confidence can and will be increased with a higher SNR of the observations. The goal of BWS is then to achieve the highest resolution with the lowest sidelobes. What is required is then a sufficiently large bandwidth and high SNR. In actual observations, sidelobes that are large but sufficiently separated in time from the central maxima can with confidence be rejected using a priori knowledge of the delay. P.W. Gorham shows in [10] a non-uniform channel spacing is preferable to a uniform channel spacing in terms of SNR and sidelobe ambiguity resolution.

## 2.4 Reference Systems and Frames

Going into this section requires a short but fundamental definition of a *reference frame* and a *reference system*. Although they are intrinsically linked, there exists a slight but important difference between the two. A *reference system* is the conceptual definition of the coordinate system, including origin and orientation together with the mathematical or physical models underlying the system. A *reference frame* is the practical realization of the reference system through various means of observations and consists of a set of identifiable and well-defined points in the sky (e.g. radio sources for the celestial reference frame) or on the planet's surface (e.g. fundamental stations for the terrestrial reference frame) [6]. This section is intended to give a brief overview of these constructions, and the role that VLBI plays in the maintenance of these fundamental systems.

In order to connect the measured quantities from geodetic VLBI (time delay and by extension, relative positions of antennas) to a larger context, there needs to be a way to place these relative measurements on a scale. This is the justification of a reference system; in order to make sense of a local measurement of position or movement, it needs to be related to a stable and accurate reference, on a scale much larger than the measurement itself. The definition and maintenance of this reference frame is one of the main tasks of modern geodesy, both traditional methods as well as those based on astronomical observations, space geodesy. The precision of the reference frames allows for accurate study and modelling of Earth dynamics, such as sea level changes, plate tectonics and in the longer run, a better understanding of the planet [12].

### 2.4.1 The Celestial Reference Frame

Using the distant stars as a reference for navigation and time-keeping has been done for millenia, before the advent of accurate technology. From those humble beginnings, the use of such *celestial* reference frames have grown to become of utmost importance when studying both distant objects as well as geophysical phenomena on Earth. From the use of optical telescopes, producing reference frames with source position accuracy of roughly a tenth of a second of arc to the advent of VLBI with the capacity of accuracy on the order of milliseconds of arc and even submilliseconds of arc starting in the late 20th century, the consequent increase in accuracy of the reference frames derived from these measurements has allowed for studies of celestial dynamics and geophysical phenomena with an accuracy not seen before. From earlier observations, using stellar sources within our own galaxy, care must be taken to accurately specify the motions of the stellar objects, since these objects exhibit detectable motions. Comparatively, the underlying principle behind a reference frame defined by objects outside our own galaxy is principally relatively straightforward; On a large enough scale, the universe is stationary, and by extension, so are distant objects to a large extent. A reference frame defined by the positions of such extragalactic sources is said to be a quasi-inertial frame, with a very low or no time-dependent motion compared to intragalactic sources [13].

The celestial reference frame currently in use is the so-called second realization of the International Celestial Reference Frame (ICRF2) derived from almost 30 years of VLBI observations. The reference frame contains precise positions of more than 3400 compact extra-galactic sources. It shall be noted that one of the main drawbacks of this realization of the reference system is the fact that many of the participating observatories are located on the northern hemisphere, leading to reduced sky coverage on the southern hemisphere [14]. The celestial reference frame is used to specify the position of celestial objects, such as satellites, stars, galaxies and so on, and several coordinate systems can be used in conjunction with the celestial reference frame. For the context of this thesis, and based on how source coordinates are specified in VLBI, the so-called Equatorial coordinate system is used. The definition on this coordinate system will be given below, as well as how to convert from celestial source coordinate to local azimuth and elevation values for telescope pointing.

#### 2.4.1.1 Celestial Coordinates

The equatorial coordinate system places the origin of the reference frame at the center of the earth, but is fixed relative to the celestial poles and the *vernal equinox* (also known as *Spring equinox*, i.e. the point in space and time where the sun's rays impact the earth orthogonal to the equator). The coordinate system divides the celestial sphere into two equal hemispheres. In the case of equatorial coordinates, this division is done in the equatorial plane of the Earth, making the *celestial equator* and the planetary equator coincide. The poles of the coordinate system are located at  $\pm 90^\circ$  from the equatorial plane, placing the poles more or less at the planet's poles. In astronomy, the coordinates of an object are often expressed as *right ascension*,  $\alpha$  and *declination*,  $\delta$ , where the right ascension measures the angular distance of the object eastwards relative to the vernal equinox. The declination measures the

angular distance of the object perpendicular to the celestial equator, with positive angles to the north and negative to the south.

In the below figure, the geometry for converting between equatorial coordinates to local horizontal coordinates is displayed. In the figure, at declination  $\delta$  and  $H$  being equal to the local sidereal time, LST, minus the right ascension,  $\alpha$ , converted from hours to degrees.  $P$  indicates the celestial pole, and  $Z$  indicates the local azimuth, respectively. The angle at  $Z$  is  $360^\circ - A$  where  $A$  is the azimuth of the object at  $X$ . If it can be assumed that the observer latitude,  $\varphi$  and LST is known, as well as  $\alpha$  and  $\delta$ , the elevation  $\epsilon$  and azimuth  $A$  can be solved for using equations 2.10-2.13. Solving for  $\epsilon$  using the cosine and sine rule for spherical trigonometry yields

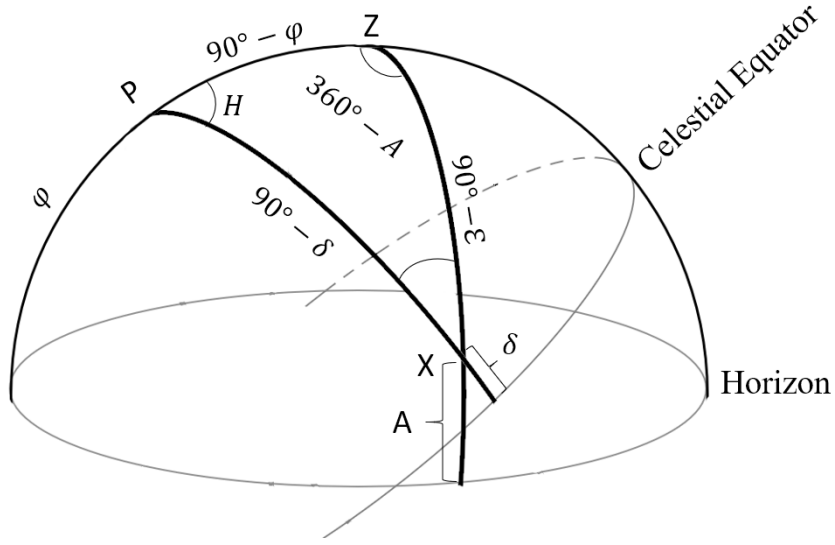


**Figure 2.3:** Figure showing the geometry required to determine the position of a celestial object based on its right ascension and declination. The horizon refers to the local horizon of the observer.

$$\begin{aligned}\cos(90^\circ - \epsilon) &= \cos(90^\circ - \delta) \cos(90^\circ - \varphi) + \sin(90^\circ - \delta) \sin(90^\circ - \varphi) \cos(H) \\ &= \sin(\delta) \sin(\varphi) + \cos(\delta) \cos(\varphi) \cos H,\end{aligned}\tag{2.10}$$

$$\epsilon = \sin^{-1}(\sin(\delta) \sin(\varphi) + \cos(\delta) \cos(\varphi) \cos H),\tag{2.11}$$

$$\begin{aligned}\frac{\sin(360^\circ - A)}{\sin(90^\circ - \delta)} &= \frac{\sin H}{\sin(90^\circ - \epsilon)} \\ &= -\frac{\sin A}{\cos \delta} = \frac{\sin H}{\cos \epsilon},\end{aligned}\tag{2.12}$$

$$A = \sin^{-1}\left(\frac{\cos \delta}{\cos \epsilon} \sin H\right).\tag{2.13}$$

### 2.4.2 The Terrestrial Reference Frame

The terrestrial reference frame is a rotating coordinate system connected to the Earth's surface and moving with it. The terrestrial reference frame defines and is useful for problems on or near the planet's surface. Traditionally, the terrestrial reference frame was realized mostly through national conventions. In 1895, the International Latitude Service (ILS) was formed, with the intentions of using globally distributed stations to monitor and define the dynamics of the frame. This group led to the formation of the International Polar Motion Service (IPMS) in 1962, and the establishment of the International Earth Rotation Service (IERS) in 1988. This development shifted the responsibility for establishing and maintaining the reference frame to a single international authority. This was the beginning of the International Terrestrial Reference Frame (ITRF) [12].

Unlike the ICRF, four different space-geodetic techniques are involved in the realization of the International Terrestrial Reference System (ITRS). These include satellite laser ranging (SLR), the global positioning system (GPS), and Doppler orbit determination and radio positioning integrated by satellite (DORIS), and finally Very Long Baseline Interferometry (VLBI). Data from these techniques come from many locations globally, containing stations for one or more of these techniques. In addition to these space geodetic techniques used, the frame also requires local-tie measurements of co-located systems, in order to realize a single unified frame, instead of four different frames from four different systems. [12], [6].

## 2.5 Timekeeping in a VLBI Context

In addition to the establishment of reference frames together with other types of instruments and techniques, geodetic VLBI alone also allows for the measurement of the rotation of Earth relative to the CRF, and with that, time. This measurement is then related to Coordinated Universal Time (UTC) by measuring the time at each telescope relative to UTC using a GPS clock at each telescope. Further, the time accuracy required is achieved by using a hydrogen maser generating a reference frequency that is used to append a timetag to each individual sample on each telescope. The reference frequency generated by the hydrogen masers essentially need to be stable in both short- and long-term perspectives. In the short term, typically the about 30 seconds per scan, an Allan deviation of  $10^{-14}$  at 30 seconds is deemed stable enough to prevent loss of coherence at the higher observation frequencies. Similarly, at longer time scales, the noise induced by temporal variations in the reference frequency derived time-base should not exceed a few picoseconds, well under the per-scan uncertainty in delay. At this time scale, the stability should be better than approx.  $10^{-14}$  at 1200 seconds [9].

## 2.6 Correlator Operations

This section is intended to introduce and explain various relevant operations performed by the correlator. These operations are general, regardless of type of cor-

relator. This section will describe these operations from a theoretical and general standpoint, with a basis in reality, whereas Section 3.3 will elaborate upon these in the context of the actual software correlator utilized at the Onsala Space Observatory.

### 2.6.1 Correlator Architectures

In terms of correlator methodology, two main fundamental approaches are used, and in principle comes down to the order of operations. An FX correlator such as the one used at Onsala Space Observatory, performs a Fast Fourier Transform (FFT) before the complex amplitudes for each frequency and antenna are multiplied to form the cross power spectra. In contrast, an XF or *lag* correlator instead first performs the cross-multiplication followed by a Fourier transform. Since a large part of the total computations are done at the Fourier transform, the FX architecture has a slight advantage over the XF architecture, at least for larger arrays, with the number of computations being largely proportional to the number of antennas as opposed to the number of antenna pairs as is the case in the XF correlator [5]. In the case of the cluster at Onsala Space Observatory used in this thesis work consists of three telescopes and three baselines, there would be no difference in computation time based on this if an XF correlator was to be used. However, the software used at the observatory is of FX-type, and as such is the one used. This text will not analyze the performance between traditional hardware correlator systems and software correlators such as DiFX, used at the observatory. For a more in depth comparison of the two philosophies, refer to the work done by Deller in [15] and Roger Capallo at the Haystack Observatory [16].

#### 2.6.1.1 Antenna Based Operations

These operations are performed on the data recorded from each individual telescope in the experiment prior to any baseline operations.

##### Alignment of data streams

Because the experiments performed with VLBI generally are extended in time, the geometry presented in Fig. 2.1 is not a constant throughout an experiment. As a consequence of this, the difference in path length and therefore the time delay between the telescopes changes during the experiment. One of the tasks of the correlator is to align the recorded data streams and align them in time, while at the same time compensating for the changing geometry of the measurement. In order to calculate this delay, the model employed takes into account many of the effects that alters the geometry of the measurement setup such as precession, nutation as well as atmospheric and oceanic loading [15]. By constantly changing the delay offset between the recorded data streams, maintaining a high correlation and getting an accurate determination of the geometric delay between telescopes becomes possible.

##### Fringe Rotation

After down-conversion to baseband, *fringe rotation* (or *fringe stopping*) is utilized to compensate for removing the effects of the sinusoidal fringe variations in the



output, as described by Eq. (2.9). The correlator output after frequency down-conversion can be written as [5]

$$V = A \cos [2\pi(\nu_{LO} + \nu_0(t - \tau_g) + (\theta_m - \theta_n) - \phi_\nu + \phi_G)], \quad (2.14)$$

where  $\theta_m$  and  $\theta_n$  are the relative phase delays introduced by the local oscillator for antennas  $m$  and  $n$ , respectively.  $\phi_\nu$  is the signal phase, and the term  $\phi_G$  is a general instrumental phase delay term. The phases for the individual antennas can be written as

$$\phi_m = 2\pi(\nu_{LO} - \nu)\tau_g + \theta_m, \quad (2.15a)$$

$$\phi_n = -2\pi\nu\tau_i + \theta_n, \quad (2.15b)$$

where  $\tau_g$  and  $\tau_i$  are geometrical and instrumental delays, respectively.

To control the frequency of this variation, an offset phase is introduced into the equation. The fringe frequency can be reduced to zero, theoretically, by varying the term  $\theta_m - \theta_n$  such that the term  $[2\pi\nu_{LO}\tau_g + (\theta_m - \theta_n)]$  remains constant, modulo  $2\pi$ . For a typical VLBI setup, the fringe rate  $\frac{d\tau_g}{dt}$  is on the order of a few hundred kHz [15].

### 2.6.1.2 Baseline-based Operations

For each baseline, the Fourier transformed time series of data from each telescope is cross-multiplied according to

$$X = V_1 V_2^*, \quad (2.16)$$

where  $V_2^*$  is the complex conjugate of the frequency domain data from telescope "2". This data, known as "visibilities" is then complex added (accumulated) until a set accumulation time is reached, thus presenting the final correlated data.

## 2.7 Post-correlator Operations - Fringe Fitting

Even though the data has already been correlated with the help of an a priori model of the parameters relevant for the experiment, some errors still exist which present themselves as non-zero residuals of the delay and delay rate observables. Source positions are not perfectly defined, and are subject to variation in both time and frequency, whereas atmospheric properties generally vary over time, and in some respects unpredictable. By making incremental changes to the group delay and delay rate, *fringe fitting* allows for the removal of much of the residual signal [16]. Fringe fitting also allows for compensation of the change in phase that the various parts (cables, feed horns, filters etc.) of the instrument induce to the signal. This process is described more in detail in Eq. (3.1). The output of the fringe fitting operation are the fringes, showcased in Fig. 2.2, and more importantly, the set of observables that are of interest: amplitude, phase, delay and delay rate of the observation.

## 2.8 Parameter Estimation in $\nu$ Solve

Up until this point, each operation is performed on a scan-by-scan basis. In order to accurately estimate and calculate the quantities of interest such as baseline length or station coordinates, an experiment must be analysed in its entirety. In principle, the individual solutions for each scan as described in Section 2.7 above, are to be combined into format suitable for the task. In practice at OSO, the data is converted into *vgosDB*, a format developed specifically for geodetic VLBI by the International VLBI Service for Geodesy and Astronomy (IVS) [17]. For the analysis of this database, parameter estimation is performed in  $\nu$ Solve, developed by NASA's Goddard Space Flight Center (GSFC), which allows for a least-squares approach to adjust for such properties as tropospheric delay and clock offsets that typically are not constant during the time of an experiment by considering them to be stochastic variables. By modelling the obtained data as

$$\mathbf{A}x + \mathbf{B}y + w = l, \quad (2.17)$$

where  $\mathbf{A}$  is the matrix containing the partial derivatives for the "constant" parameters,  $x$ ,  $\mathbf{B}$  the matrix containing the partial derivatives of the "stochastic" parameters  $y$ ,  $w$  a vector of random errors and  $l$  is the vector containing the observed,  $O$  minus the modelled,  $C$ , values. Following a standard approach, the goal is to minimize the function

$$S = w^T Q_w^{-1} + y^T Q_y^{-1} y, \quad (2.18)$$

where the a priori covariance matrices  $Q_w$  and  $Q_y$  can be calculated based on the properties of respective stochastic processes like knowledge of clock drifts and atmospheric tendencies.

The two vectors  $\vec{x}$  and  $\vec{y}$  can be estimated according to

$$\vec{x} = [A^T(BQ_y B^T + Q_w)^{-1}A]^{-1}A^T(BQ_y B^T + Q_w)^{-1}l, \quad (2.19)$$

$$\vec{y} = Q_y B^T (BQ_y B^T + Q_w)^{-1}(l - A\vec{x}). \quad (2.20)$$

Calculating  $\vec{x}$  is necessary in order to calculate  $\vec{y}$ . Having done so, the post-fit residual can be written as

$$\varepsilon = l - A\vec{x} \quad (2.21)$$

and the normalized chi-squared parameter can be written as

$$\sigma_0^2 = \frac{\varepsilon^T (Q_w + BQ_y B^T)^{-1} \varepsilon}{N - n}, \quad (2.22)$$

where  $N$  is the number of observations (order of hundreds or thousands depending on length of experiment) and  $n$  is the number of estimated parameters. As an example, if one were to estimate only station positions in an  $X, Y, Z$  coordinate system, one would need to estimate nine parameters (three for each telescope). The software  $\nu$ Solve allows for any combination of estimated parameters including clocks, tropospheric characteristics and station coordinates [18].

# 3

## Methods

In order to achieve valid measurements, the observations for the baseline between the two twin telescopes, as well as the baselines between the 20 metre telescope and either of the two twin telescopes need to be performed at the same frequencies, and ideally the same bandwidth. As initial analysis showed, the  $S$  frequency band was seen to be heavily contaminated by RFI and will as such not be used. The operational considerations and setups will be described in this section, together with some intermediate results obtained during early experimentation to guide future experiments.

### A Note on Terminology

A short primer on the terminology used in the context of this work is here provided to avoid any confusion for the reader. An *experiment* refers to an entire set of discrete measurements of radio sources ranging in time from a few seconds to several minutes depending on the requirements for good SNR. The experiments themselves are named after the year and day of year the experiment takes place. For instance, an experiment performed on the first of January of 2019 could be named **K19001** where K is a prefix to distinguish it from other experiments, 19 is the year, and 001 signifies the first day of the year. Each individual measurement is referred to as a *scan* or *observation*. The names used for the telescopes are as follows: The twenty metre telescope can, and will be referred to as the *20 metre*, *On* or *ONSALA60* depending on the circumstance. Similarly, the two twin telescopes are referred to as either *The Twin Telescopes* or *OTT* when referring to both telescopes, and *Oe* or *ONSALA13NE* for the easternmost of the two, whereas the westernmost telescope is referred to as either *Ow* or *ONSALA13SW*. These names come from log and configuration files, and all of them are used in some context or other. In order to maintain consistency with the various softwares used in the course of this thesis work, the baselines between the telescopes are referred to as LW, LX and XW for the baselines between the twin telescopes, Oe and On, and Ow and On, respectively. Again, this nomenclature comes from various evaluating softwares, and is maintained for consistency's sake.

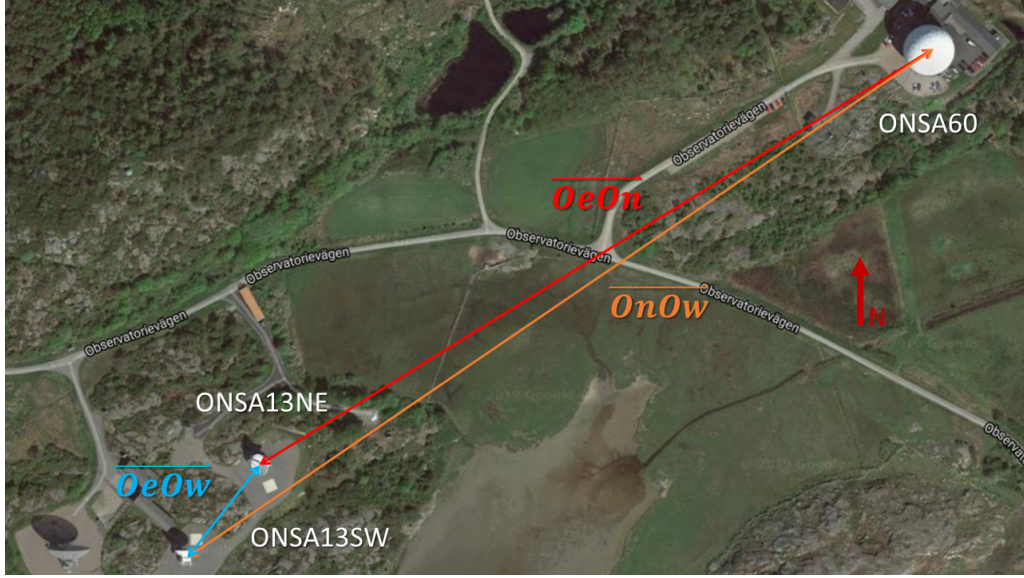


**Figure 3.1:** Overhead screenshot from *Google Maps* of the telescopes and baselines utilized in the course of this thesis work.

## 3.1 Baseline Measurements Between the two Twin Telescopes

In principle, the full VGOS configuration can be used when performing baseline measurements on the OTT baseline. However, due to the short baseline involved, sufficient accuracy can be achieved using a narrower frequency band. Further, during early evaluation it was discovered that the lower frequency band(s), most notably the *S* and to some extent the *C* bands were heavily corrupted by either RFI or internal system noise.

## 3.2 Baseline Measurements Between the OTT and the 20 Metre Telescope

Due to the fact that the antennas and receivers associated with the Twin Telescopes and the 20 metre telescope, in short, are different, a different approach to the VGOS setup needed to be defined, tested and evaluated. In order to perform interferometry, the telescopes involved in any baseline measurements need to be configured with identical settings w.r.t. frequency selection and bandwidth. Since the Twin Telescopes are inherently designed to be extremely broadband for the VGOS system, whereas the 20 metre telescope is not, the setup needs to be made with the 20 metre as reference. For geodetic measurements in the *X*-band, the legacy *S/X* in its default configuration system allows for recording of 8 simultaneous channels each with 16 MHz bandwidth, and using channel spacing and *bandwidth synthesis*, a 720 MHz spanned bandwidth can be realized.

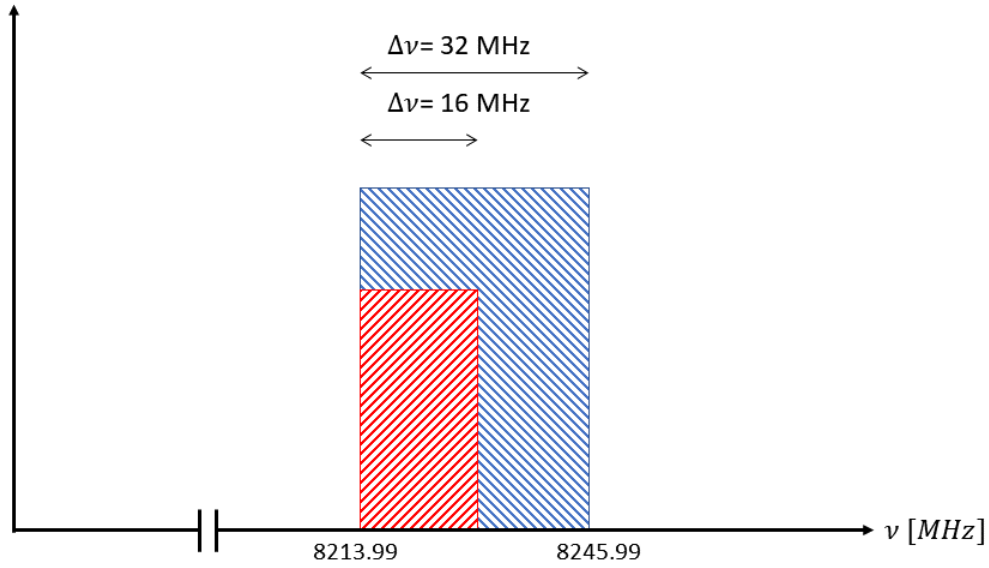


**Figure 3.2:** Example of a recorded X-band Channel and the different bandwidths of the different telescopes. The narrower red box corresponds to the On telescope and the broader red box corresponds to the OTT. The height of the boxes are irrelevant and only for clarity.

The frequency setup initially used for baseline measurements between the telescopes at the observatory for the 20 metre telescope is presented below.

**Table 3.1:** Eight-channel frequency setup used for the experiments performed in this master’s thesis

$\nu$ , MHz	$\Delta\nu_{On}$	$\Delta\nu_{OTT}$ , [MHz]	$LO_{On}$	$LO_{OTT}$ , [MHz]	$SB_{On}$	$SB_{OTT}$	$Pol_{On}$	$Pol_{OTT}$
8213.99	16	32	8080	11600	USB	LSB	RHCP	Dual X+Y
8253.99	—	—	—	—	—	—	—	—
8353.99	—	—	—	—	—	—	—	—
8513.99	—	—	—	—	—	—	—	—
8733.99	—	—	—	—	—	—	—	—
8853.99	—	—	—	—	—	—	—	—
8873.99	—	—	—	—	—	—	—	—
8933.99	—	—	—	—	—	—	—	—

In Table 3.1 above, the column  $\nu$  signifies the frequency at which the individual bands start. The table reveals some differences between the two types of telescope. First of all, the recorded channel bandwidth of the OTT is twice that of the older On telescope. This requires a cropping of the recorded frequency bands of the OTT, to match that of On. Using the built-in *zoom* functionality of *DiFX* allows for this cropping to be made easily. The arrangement of an example channel is shown in Fig. 3.2 and is similar for all involved bands.

### 3.2.1 New Firmware on the Digital Baseband Converter (DBBC)

In May of 2019, a new firmware was installed on the DBBC2 connected to the 20 metre telescope at the observatory. For this work, the most relevant change this

implied was the possibility to use a larger channel bandwidth of 32 MHz compared to the previous 16 MHz. In principle this means that the receiver of the 20 metre telescope should perform similar to the twin telescopes, disregarding any polarization mismatch. Starting from the experiment named **K19135**, the observations were made using this broader channel bandwidth and a comparison of the results between the "legacy" setup and the newer setup will be performed.

## 3.3 Data Recording and Processing Workflow

The following chapter describes the general flow of data, which programs are used and any special considerations needed. It shall also be noted that the work flow is identical, regardless of the type of observation, be it a one hour intensive or a 24 hour session. The text will be kept somewhat general, since the actual available hardware and software used at other observatories may or may not differ compared to the setup used at Onsala.

### 3.3.1 Recording

After having passed through the receiver front end, the signal is passed onto the Digital Baseband Down Converter (DBBC). This purpose built machine is responsible for converting the IF signal from the front end down to baseband and digitizing the signal. In the case of these experiments, 2-bit sampling is used, and as will be shown later on, different channel bandwidths can and will be used. After being downconverted and digitized the recorded data is transferred to the *FlexBuff* system and saved on traditional hard disk drives.

### 3.3.2 Processing

After the signal from the telescopes has been digitized and recorded on the *FlexBuff* system, it is transferred to the working directory of the processing unit. At this point, depending on the type of experiment, which telescopes are involved in the experiment, which frequency bands that are of interest or if any particular observations of the experiment are to be excluded, the control files for the correlator may or may not be altered. The control files themselves are easily modified using any common terminal text editor such as *GNU nano* or *vi*. Some scripts designed to simplify this workload are provided as part of this thesis, as well as working examples of these control files for the local-tie measurements performed at OSO. It is of vital importance that the *\*.vex* and *\*.v2d* file contains information on frequency setup, data format for the recorded data, scan and source information. To provide the correlator with *a priori* data for the model calculations, the control files also contain antenna parameters, location and clock offsets, as well as Earth orientation parameters.

The *DiFX* correlator requires additional files for running. Helper programs included in the software generate these files based on the information contained in the *\*.v2d* and *\*.vex* files, and should ideally not require editing by the operator, however they can be in the case of poorly configured control files. The *DiFX* software then creates

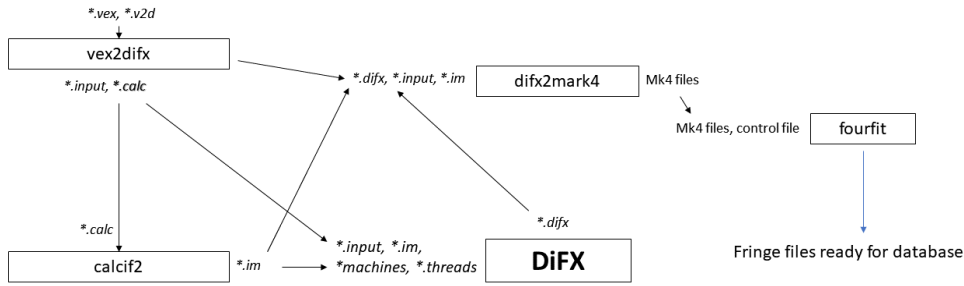


**Figure 3.3:** Block diagram of correlator workflow showing what files are being generated and used in what instance. *Italics* show file endings, and regular block letters show file types.

a set of correlation coefficients for each individual scan. In order to maintain file system consistency, the *DiFX* software converts the correlation coefficient files using *difx2mark4* built into the software suite, to the *Mark4* format used in legacy geodetic VLBI. The general workflow of the correlating procedure is shown in Fig. 3.3. File lists are defined in the \*.v2d file, and points to VDIF files associated with the experiment being correlated.

The obtained fringe files for each baseline and scan are then exported to a geodetic VLBI database, in this case *vgosDB* and analyzed in the least-square solver *νSolve*.

### 3.4 Phase Corrections

Because the signal is received on discrete units with potentially different signal paths, there arises a need to understand the behaviour of the system in terms of its effects on the signal phase. One method of doing so, and which is commonly used in VLBI is the use of phase calibration tones spaced out in some interval injected into the front end of the telescope receiver. By extracting these tones and analysing their phase, the per-channel phase delay can be determined. In the case of the legacy *S/X* system, these tones are separated by 1 MHz and in the case of *VGOS*, they are separated by 5 MHz [9],[19]. Using this method is convenient, due to its semi-automatic nature and full support in the software used at many observatories, such as *OSO*.

When performing *bandwidth synthesis* measurements with individual frequency band spaced out to cover a maximum allowable bandwidth as described in Section 2.3, it was during early experimentation discovered that the calibration pulses injected into the signal path at the receiver had a tendency to strongly correlate in the evaluation of the scans. This behaviour is exemplified in Fig. 3.4. It was therefore decided to instead implement *manual phase calibration* in order to connect the phases of the individual channels. This section is intended to describe the method used for the experiments performed in the scope of this masters thesis.

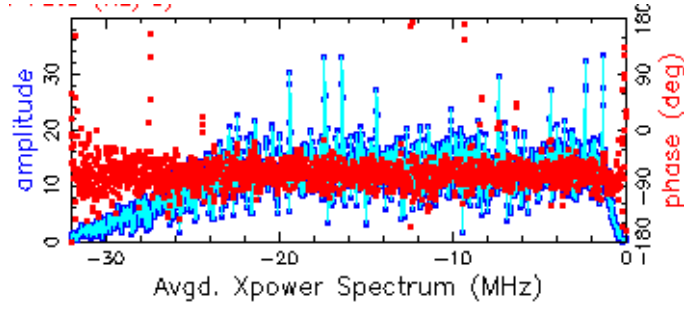


**Figure 3.4:** Correlated phase calibration tones in the X-band on the LW baseline

### 3.4.1 Phase Stability

In order for manual phase calibration to be valid, it is required that the receiver systems (i.e. the antennas, front- and backends and any auxillary systems) are phase stable over a longer period, preferably over entire experiments. In essence, this means that the relative phase difference between two adjacent channels is approximately constant over the entire experiment. In order to verify this and proceed with manual phase referencing, a number of scans with a high SNR was selected from the experiment **K19120** and the relative phases of each channel were extracted and analysed. It was found that the relative phase difference across all baselines and frequency channels was approximately constant, allowing for manual phase calibration. The table below shows the difference in phase across the frequency bands for a number of scans in experiment **K19120**.

**Table 3.2:** Difference of phases in degrees between frequency channels for some high-SNR scans in experiment *K19120*

$\Delta\phi_i$	i = 1	i = 2	i = 3	i = 4	i = 5	i=6	i = 7
Scan #1	227.5	68.6	244.1	124.4	218.8	22.4	109.4
Scan #2	229.3	63.3	234.4	108.1	216.3	14.7	104.5
Scan #3	233.7	69.4	241.9	121.9	217.3	21.2	108.9
Scan #4	228.6	58.6	228.5	103.5	207	20.9	84.3
Scan #5	229.6	73.8	250.4	130	223.6	23.5	110.7

As can be seen in the above table, the difference in phase between frequency channels differs at most about  $10^\circ$ , and the system is deemed phase stable. The phase stability displayed above for experiment *K19120* was exhibited by the system for consequent experiments, although they will not be presented here.

### 3.4.2 Manual Phase Calibration

The manual phase calibration performed on consecutive experiments is relatively straight forward, but require some knowledge on what is being done and how the various kinds of software handle phase correction. The *fourfit* package supports directly modifying the phase of any number of recorded channels for any arbitrary scan or an entire experiment by introducing an offset. Ideally, the phase calibration



tones injected in the front end of each telescope should be used to gauge the effect of the instrumental phase offset. However, as described earlier, this is not possible due to the risk of autocorrelated pulses. Instead, a source with close to ideal geodetic VLBI properties, i.e. small angular extent in the frequency band of interest and high signal strength is selected. Consulting available documentation, as well as the different sources that were actually observed for a given experiment, the radio source known as **NRAO150** was selected as a phase reference. At X-band, this source is smaller than one milliarcsecond in angular size, and produces a signal strength of a few Janskys [20]. By using such a source, it can be assumed that the recorded phase is dominated by the phase of the source and that no effects such as different phases due to the spatial extent contaminates the recording. The observed phase, which should be continuous across all recorded phases of interest, is then used as a reference phase for the entire experiment. If the recorded phase of a scan  $i$  can be written as

$$\phi_i = \phi_s^i + \phi_{inst}^i + \phi_{pos}^i + \phi_{ant}^i + \phi_{tropo}^i + \phi_{iono}^i, \quad (3.1)$$

where  $\phi_s$  is the phase of the source,  $\phi_{inst}$  the phase error due to the instrumentation,  $\phi_{pos}$  and  $\phi_{ant}$  are geometrical phase errors stemming from source and antenna position uncertainty and  $\phi_{tropo}$ ,  $\phi_{iono}$  are the phase errors stemming from the troposphere and ionosphere, respectively. If the errors due to instrumentation and geometrical uncertainties can be assumed to be at least constant over the time of an experiment (i.e.  $\Delta\phi_{inst}, \Delta\phi_{pos}, \Delta\phi_{ant} = 0$ ), differentiating the phases of the reference scan  $r$  and any other scan  $i$  in the experiment should yield

$$\Delta\phi = \phi^i - \phi^{ref} = (\phi_s^i - \phi_s^r) + (\phi_{tropo}^i - \phi_{tropo}^r) + (\phi_{iono}^i - \phi_{iono}^r). \quad (3.2)$$

If the tropospheric and ionospheric effects can be accounted for, then

$$\Delta\phi = \phi_s^i - \phi_s^r, \quad (3.3)$$

essentially being a constant offset. As Fig. 3.5 shows below, manual phase calibration successfully aligned the phases in the scan **120-1908** when using scan **120-2057** as a reference, validating this method.

### 3. Methods

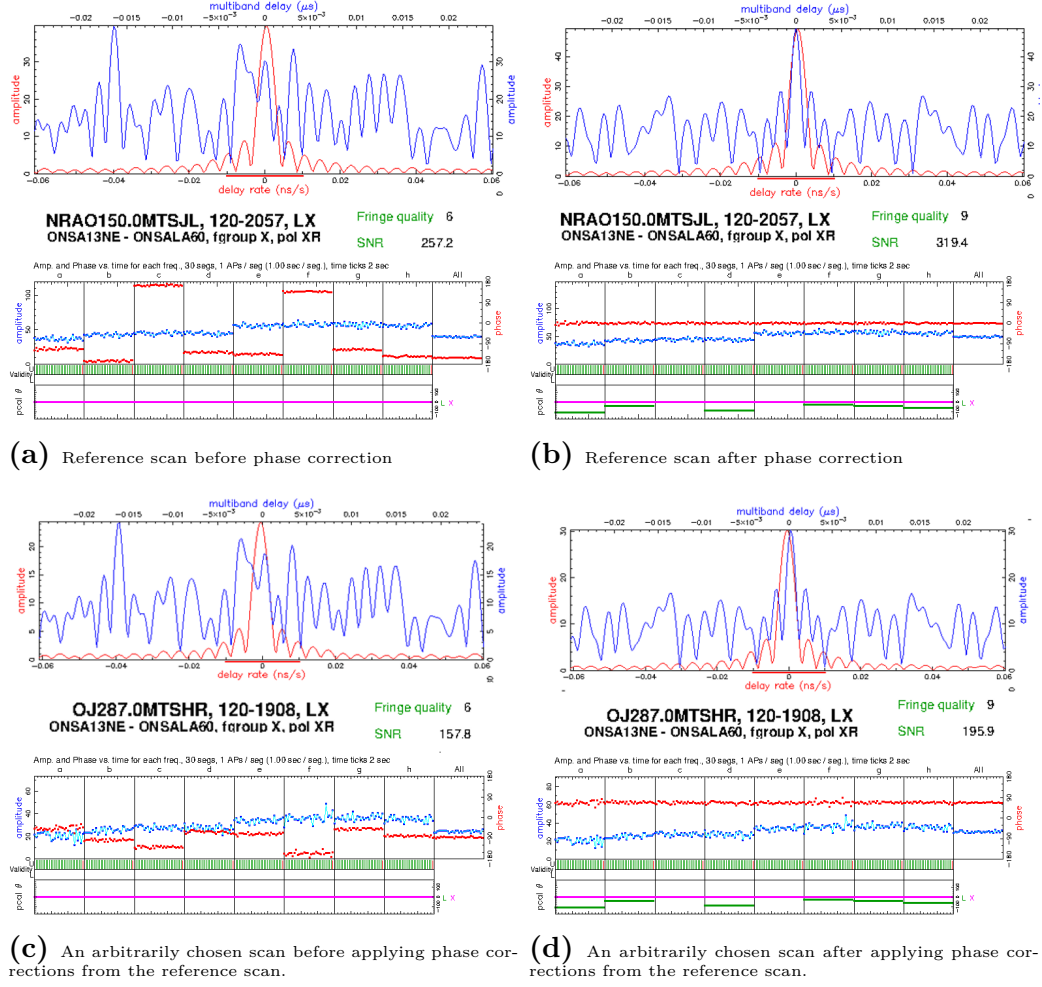


**Figure 3.5:** Comparison of fringe detections using manual phase calibration. These are *fourfit* plots cropped and edited to highlight the corrected phases, and to display differences in fringe quality and SNR. The phase offset  $\Delta\phi$  (red line in lower parts of each graph) is clearly seen in the lowermost two pictures

In the case of a relatively short baseline, such as the baselines between the telescopes at OSO (On the order of 500 metres), the errors introduced by atmospheric effects are almost completely removed, due to the telescopes more or less observe the same atmosphere for a given scan [8]. If the instrumental and positional effects on the phase can be assumed constant, their effects can then be removed from any scan by simply subtracting the phases.

#### 3.4.3 Polarization Products

In its default configuration, *fourfit* treats each recorded polarization independently, allowing for any combination of polarization to be evaluated separately, i.e. allowing the operator to individually analyze the polarization combinations XX, YY, XY or YX for the dual horizontal polarizations of the twin telescope baseline, or the RX and RY combinations of the baseline between the twenty metre telescope and either of the twin telescopes. The software also allows for any combination to be evaluated

together, i.e. combining XX and YY or RX and RY into one linear combination [16]. The total intensity  $I$ , or Stokes parameter  $S_0$  is given by

$$I = (X_a^* X_b + Y_a^* Y_b) \cos \Delta + (X_a^* Y_b + Y_a^* X_b) \sin \Delta \quad (3.4)$$

where  $a$  and  $b$  denote the two telescopes of the baseline,  $\Delta$  denotes the parallactic angles between the two, and  $*$  denotes the complex conjugate. This combination increases the total intensity, and by extension, the SNR, allowing for a more accurate result. It shall be noted that this linear combination in actuality is a pseudo-Stokes parameter, in that it is dimensionless and that any system gains and losses are set to unity [9]. Since the telescopes used in this thesis are located relatively close to each other (compared to baselines typically used in geodetic VLBI), the angle  $\Delta$  goes to zero, minimizing the cross-polar product. As a consequence for this thesis, only the co-polar products are evaluated for the twin telescopes (i.e. XX+YY) and the RX+RY products are evaluated for the baselines between the twenty metre telescope and either of the twins. In practice, this resulted in a roughly 50 % higher SNR for any given scan.

### 3.5 Tropospheric Corrections

In the log files provided to  $\nu$ Solve, a local reading of air pressure is provided. Since the refractive index is dependent on pressure, differences in pressure as seen by each telescope introduces errors in the results, if not properly calibrated for. In the case of the Onsala Observatory, all three telescopes share the same pressure gauge, which could potentially lead to some loss of accuracy. In order to evaluate the impact of this, the log files were modified using a custom made script written by the author of this report. To get an estimate of the air pressure differences between the pressure gauge and the telescopes, the following equation was used to determine the pressure at height  $h$  [21]

$$P = P_{ref}(1 - 0.0000226(h - h_{ref}))^{5.225} \quad (3.5)$$

where  $P_{ref} = 1013.25$  hPa,  $h_{ref}$  is the reference height above the reference ellipsoid and is equal to zero. The value of  $h$  is given by local surveys and is presented together with the estimated pressure in Table 3.3 below.

**Table 3.3:** Estimated air pressure difference at the Onsala Telescopes.  $\Delta P$  of the telescopes compared to the pressure gauge

Site	Height, $h$ , [m]	$\Delta P$
Pressure gauge	46.6	
On	59.3	-1.5
Ow	52.3	-0.7
Oe	52.3	-0.7

From the above table, it can be seen that the pressure value as given by the log files should be corrected by -1.5 hPa for the 20 metre telescope, and by -0.7 hPa for

the twin telescopes. This correction will be evaluated and presented alongside the results without the air pressure correction.

## 3.6 Scheduling of Observations

In principle, the local-tie vector between any two telescopes can be determined using one observation, provided a good model of atmosphere, EOP's and so on is available. However, due to the nature of the unknown variables present in an observation, multiple observations in rapid succession has to be performed. In order to achieve good results, scheduling of observations is done to achieve a good sky coverage, and to achieve a signal-to-noise ratio that is deemed high enough for high confidence position determination. Scheduling is done in the already available software package *sked* with the help of Rüdiger Haas and Armin Corbin.

## 3.7 Extended Bandwidth Using all Available Channels

As previously mentioned, the legacy *S/X* geodetic VLBI system utilized a total of 14 frequency channels of 16 MHz each, with 6 channels in the S-band and 8 channels in the X-band. In principle, the receiver could be configured to place these 14 channels in the X-band, allowing for a relatively large total bandwidth while still avoiding the RFI of the lower frequency channels. If time and observation opportunities allow, this will be investigated.

# 4

## Results

The following section will present the results of the experiments performed during the spring of 2019. Example output from *fourfit* will be presented and elaborated upon, although the main focus will be on the results obtained through  $\nu$ Solve, with the exception of the initial trial experiments performed to work out viable configurations. Each experiment will first be separately presented and examined, since differences in receiver and scheduling setup necessitates some attention. The section will be rounded off with a comparison between the results of the different setups.

### 4.1 Early Experimentation

This section is intended to demonstrate the early results from experiments, used to evaluate correct frequency and receiver setups, software configuration and so on. Due to the incomplete nature of these experiments, only the output from the correlator, the aforementioned *fringes* will be displayed and elaborated upon. The below set of pictures show the correlator output for two experiments run in the course of this master's thesis. The first show the fringes, or rather, lack thereof, as a result of incorrectly selected recording bands for the experiment run on April 2, 2019. The second show a fringe plot from the experiment run on April 30, 2019.

#### 4. Results

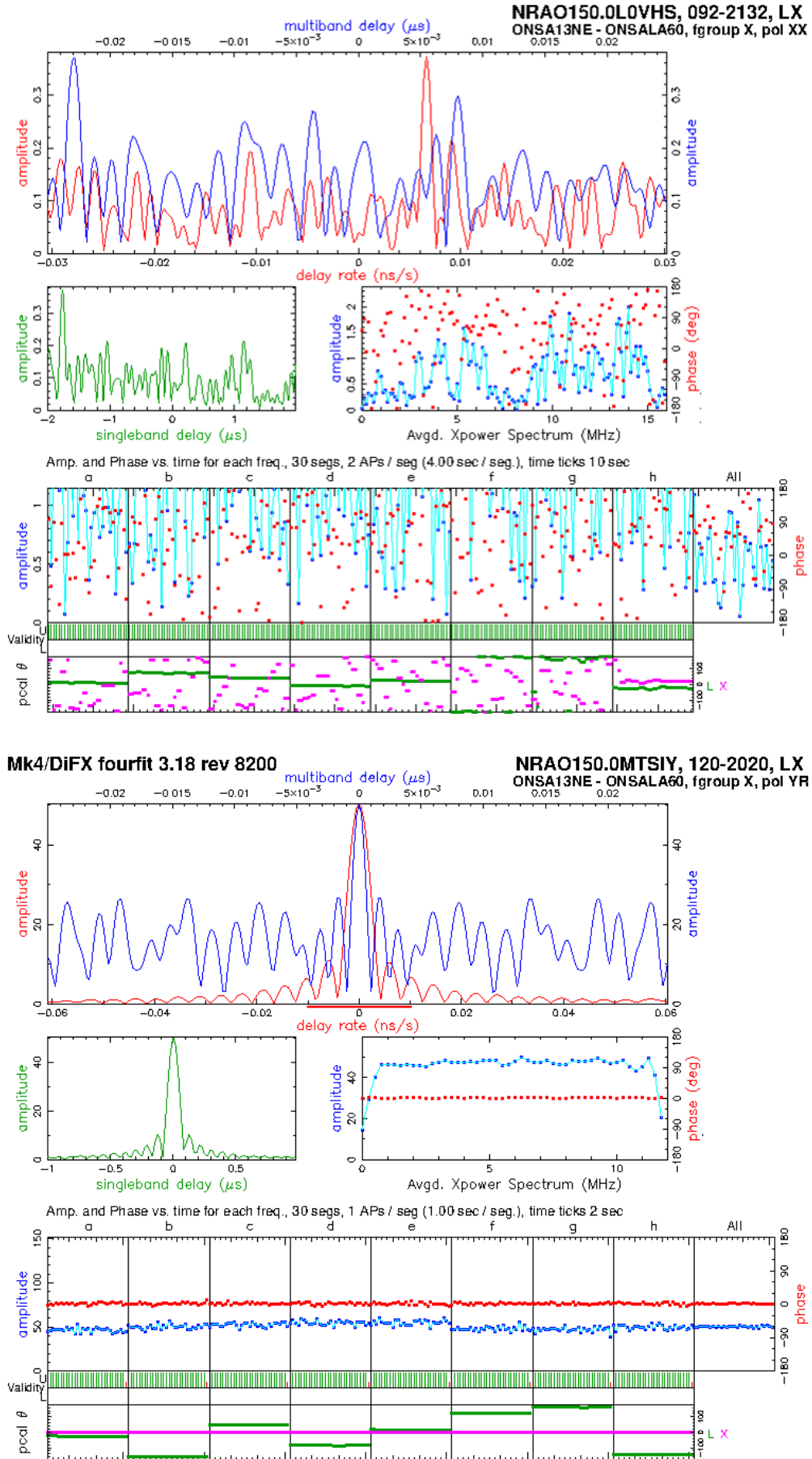


**Figure 4.1:** Fringe plots from experiments K9092c and K19120 showing a clear difference between a "bad" (upper figure) setup and a "good" (lower figure) one.

While the above plots seem crowded, they contain a lot of useful information. Starting from the top, the multiband delay and delay rate ( $d\varphi/d\theta$  in units  $\mu s$  and  $ns/s$  respectively) is shown. It is centered on zero, as the correlator measures the time lag and by applying an alignment in time, stops the fringes' apparent movement across the sky relative to the telescopes. The middle two sections display the single band delay, which can be seen to be much wider than the multiband delay peak, indicating a lower  $\nu_{RMS}$ , which is to be expected. To the right of this is the averaged cross-power spectrum for all involved frequency channels, in this case 8 of them, together with the averaged phase of the channels. Lastly, for each frequency channel, the time series of the recorded amplitudes and phases after Fourier transformation and cross-multiplication as performed by the correlator is shown. The experiences drawn from early experiments such as **K9092c** shown here guided the setup for future experiments. On their own, such plots do not necessarily tell us much of the actual observables such as  $WRMS$  or baseline lengths, but give a good indication of the overall data quality from a given experiment.

Initially, it was believed that the poor result in experiment **K9092c** and other early experiments was simply due to too short of an integration time, instead of the wrong selection of frequencies before the experiment. This is reflected in the experiment discussed in Section 4.2.1.

## 4.2 Experiments on the Onsala Telescope Cluster

The results presented in the following sections come from those experiments that resulted in longer time series that could be evaluated in  $\nu$ Solve. It shall also be noted that in these longer time series, unpredictable performance on the lowest frequency channel lead to the omission of this channel in the analysis. By using Eq. (2.3a) and 2.3b, an estimate can be given on how much the uncertainty is increased from an eight channel setup. This will be done in the concluding section of this report, to avoid cluttering the results section. To get an idea of expected performance when performing the experiments on the baselines between the older 20 metre telescope and the newer twin telescopes, the experiments performed on the Wettzell telescope cluster in 2014 and 2015, as reported by [8], being one of the only publicized experiments of this kind, gives an idea of the performance to expect. Typical residual values of about 5-10 millimetres in the X-band seem to be reasonable values to expect with this setup according to this report. This also agrees with the (albeit estimated) value for  $\sigma_\tau$  as discussed earlier in Section 2.1. An example of the delay residuals from the experiment **K19120** 24 hour session is shown in Fig. 4.2-4.4 below. The other experiments, as will be shown in tables 4.3 and 4.2, exhibit similar behaviour in terms of magnitudes and it can be seen that the baselines involving the twenty metre telescope generally are worse than the baseline between the twin telescopes.

## 4. Results

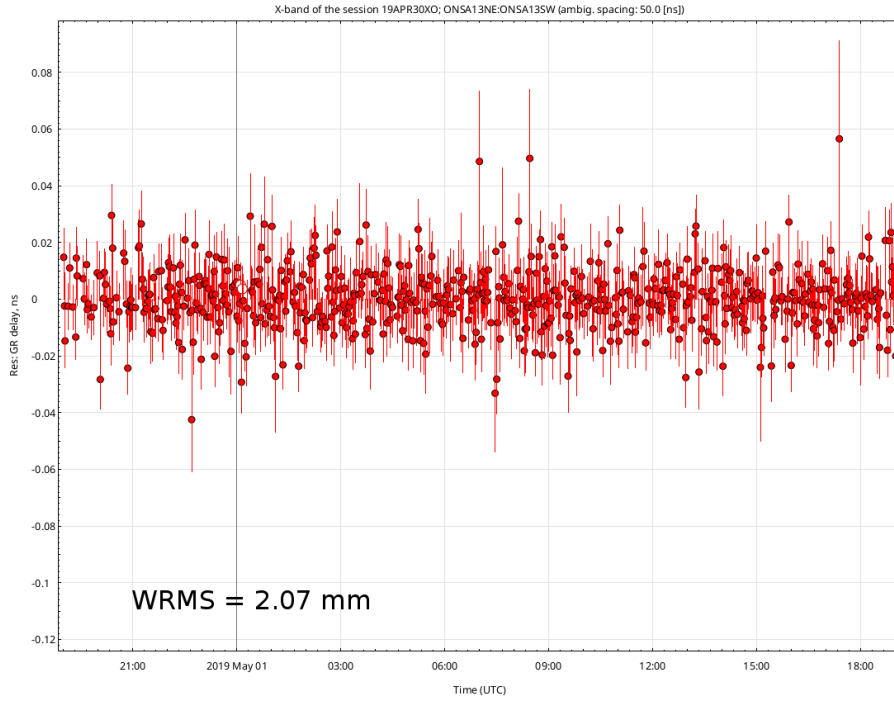


**Figure 4.2:** Multiband delay residuals on the OTT baseline from an entire 24 hour session. The delay residuals are on the order of 20-40 ps corresponding to a WRMS of 2.07 mm.

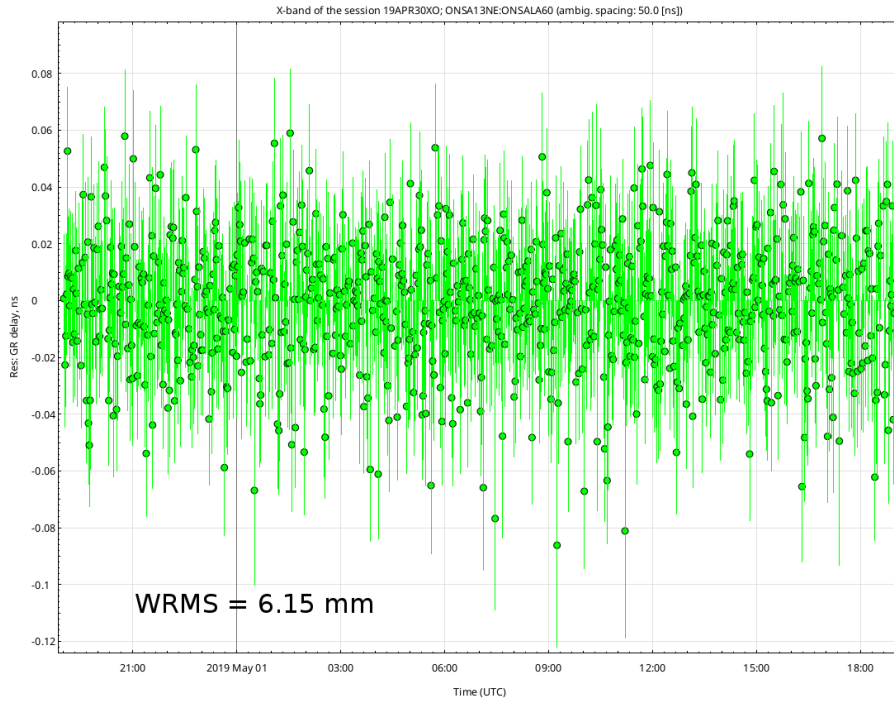


**Figure 4.3:** Multiband delay residuals on the OE-ON baseline from an entire 24 hour session. The delay residuals are on the order of 20-50 ps corresponding to a WRMS of 6.15 mm.



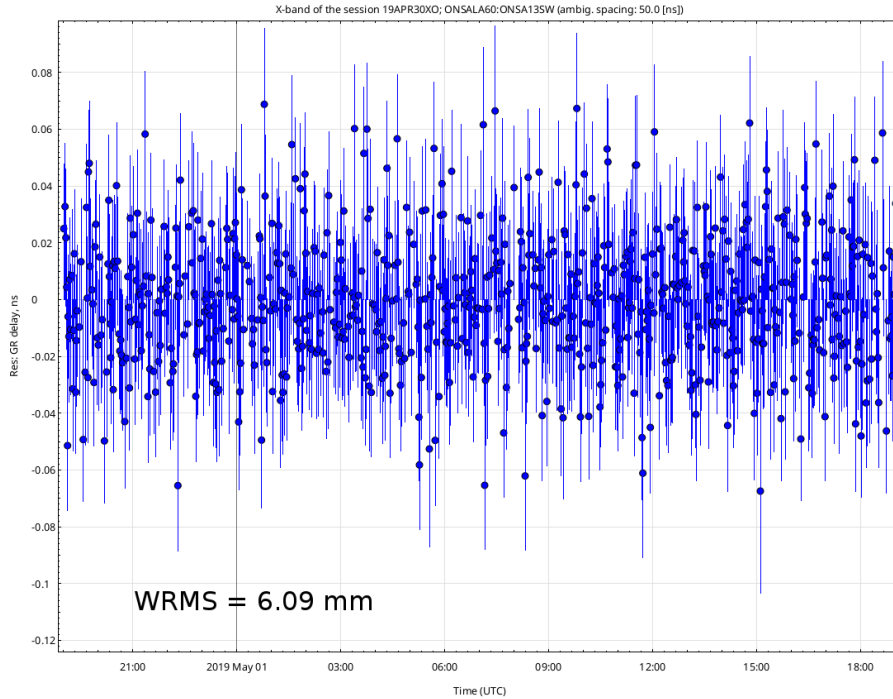


**Figure 4.4:** Multiband delay residuals on the OW-ON baseline from an entire 24 hour session. The delay residuals are on the order of 20-50 ps corresponding to a WRMS of 6.09 mm.

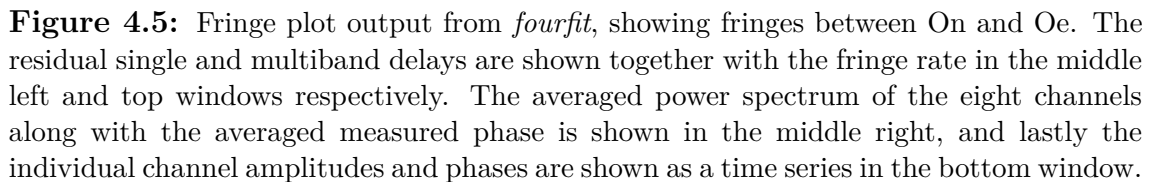
#### 4.2.1 K9092

The experiment performed on April 2<sup>1</sup> as described in Section 3.2 is considered to be the first successful experiment involving the three telescopes of the Onsala Space Observatory. Based on the faulty assumptions drawn from the experiment described in Section 4.1, it was assumed that a much longer integration time than 30 seconds per source was required for a sufficiently good SNR. As a consequence, a total of 120 seconds of integration time was used for each scan, resulting in a total of 19 scans for the entire experiment. This resulted in a generally extremely good SNR and high fringe quality, with some individual scan exhibiting a lower SNR and corresponding fringe quality. Even at the lower end, the quality of observations were generally good enough to be useful. A fringe plot on the "good" end of the spectrum is shown in Fig. 4.5 below.

The fringe data was then exported to *vgosDB* with the help of Grzegorz Klopotek at the Department of Space, Earth and Environment. Further processing in *νSolve* allows for further removal of residuals by estimating a set of parameters. Due to the lower amount of individual observations in this experiment, only clocks, troposphere and station position can be determined with low uncertainty. For the three baselines in this experiment, the *weighted root-mean-square*, *WRMS* residual is presented in Table 4.1 below together with the uncertainty,  $\sigma_\tau$ , in the time delay measurement

<sup>1</sup>The first good experiment share a date with the bad experiment as described in Section 4.1 and shown in Fig. 4.1, as on this day two different experiments with different setups were performed, hence the similar names.

as well as the baseline vector length and associated uncertainty.

Table 4.1: Results from  $\nu solve$  for experiment K9092a

It shall be noted here, that the low amount of observations for this experiment does not really allow for any further analysis, other than to see that the approach was valid. The experiences gained from this experiment would guide the setup for the upcoming experiments, as described below.

### 4.3 Results of Pressure Adjustment

The results presented here are derived from a subset of data where the recorded pressure values for each telescope was adjusted in accordance to Section 3.5 and processed in  $\nu$ Solve. The datasets analysed here are the two 24-hour sessions denoted **K19120** and **K19136**, divided into four six-hour segments and analysed.

#### 4.3.1 No Pressure Correction

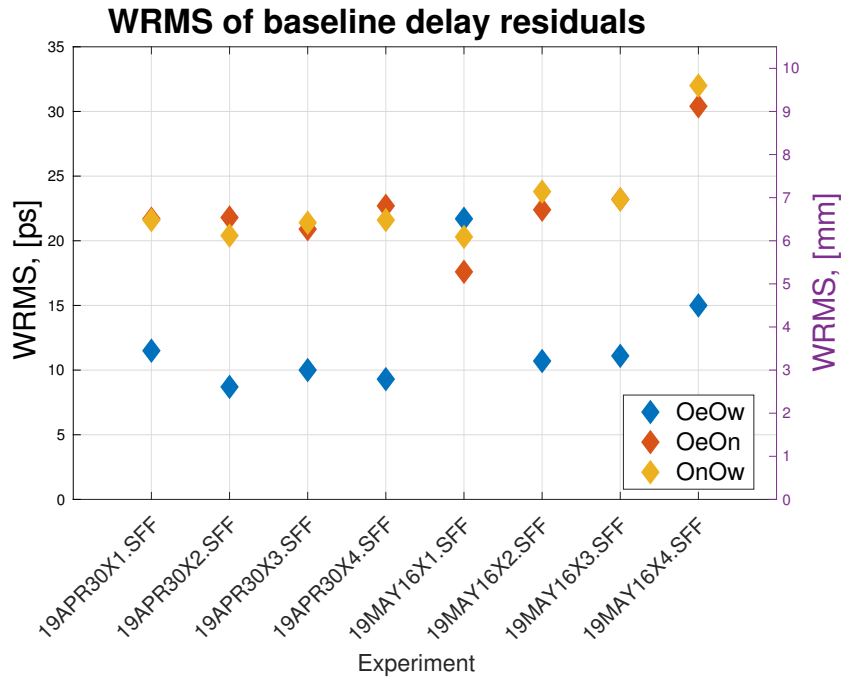


**Figure 4.6:** The WRMS of all experiments, with no correction made for air pressure

**Table 4.2:** WRMS of baseline residuals for each evaluated session in mm, together with the baseline lengths in metres, with uncertainty in mm. No additional pressure correction in log files for  $\nu$ Solve

Session	WRMS,  LW LX XW  [mm]	LW [m]	LX [m]	XW [m]
K19120 <sub>1</sub>	3.45   6.51   6.48	74.9611 ± 1.91 mm	468.6819 ± 2.64 mm	540.3118 ± 2.62 mm
K19120 <sub>2</sub>	2.61   6.54   6.12	74.9605 ± 1.31 mm	468.6828 ± 2.32 mm	540.3128 ± 2.30 mm
K19120 <sub>3</sub>	3.00   6.27   6.42	74.9607 ± 1.61 mm	468.6847 ± 2.46 mm	540.3142 ± 2.49 mm
K19120 <sub>4</sub>	2.79   6.81   6.48	74.9611 ± 1.54 mm	468.6809 ± 2.59 mm	540.3123 ± 2.54 mm
K19136 <sub>1</sub>	6.51   5.28   6.09	74.9620 ± 2.42 mm	468.6795 ± 1.94 mm	540.3100 ± 2.19 mm
K19136 <sub>2</sub>	3.21   6.72   7.14	74.9611 ± 1.47 mm	468.6830 ± 2.09 mm	540.3115 ± 2.17 mm
K19136 <sub>3</sub>	3.33   6.96   6.96	74.9614 ± 1.62 mm	468.6833 ± 2.36 mm	540.3118 ± 2.37 mm
K19136 <sub>4</sub>	4.50   9.12   9.60	74.9605 ± 2.24 mm	468.6833 ± 3.04 mm	540.3135 ± 3.18 mm
Weighted averages & sigmas:		74.9611 ± 0.21 mm	468.6822 ± 0.50 mm	540.3121 ± 0.46 mm

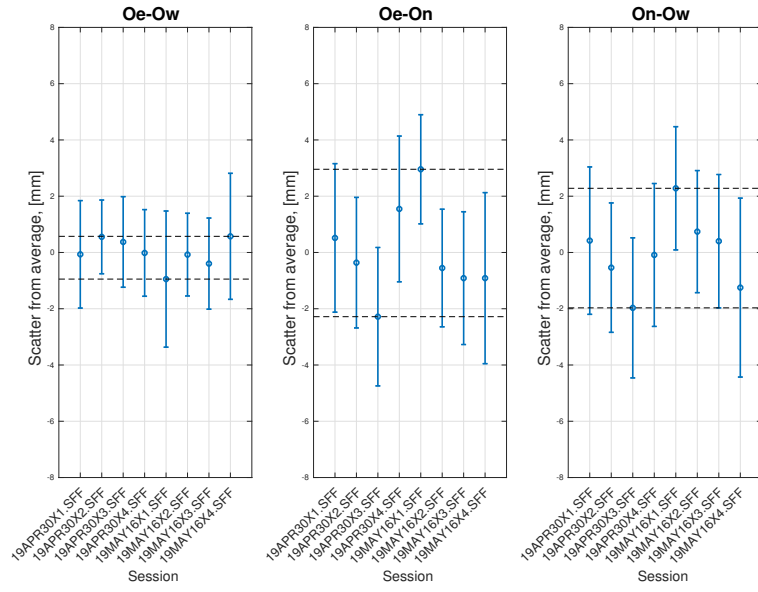


**Figure 4.7:** Plots of scatter around the average baseline length, calculated from all included sessions. Scatter in mm along the y-axis and session name on the x-axis. The dashed lines represent the maximum and minimum scatter, respectively.

### 4.3.2 With Pressure Correction

These results include the corrections detailed in Table 3.3 to the pressure readings.

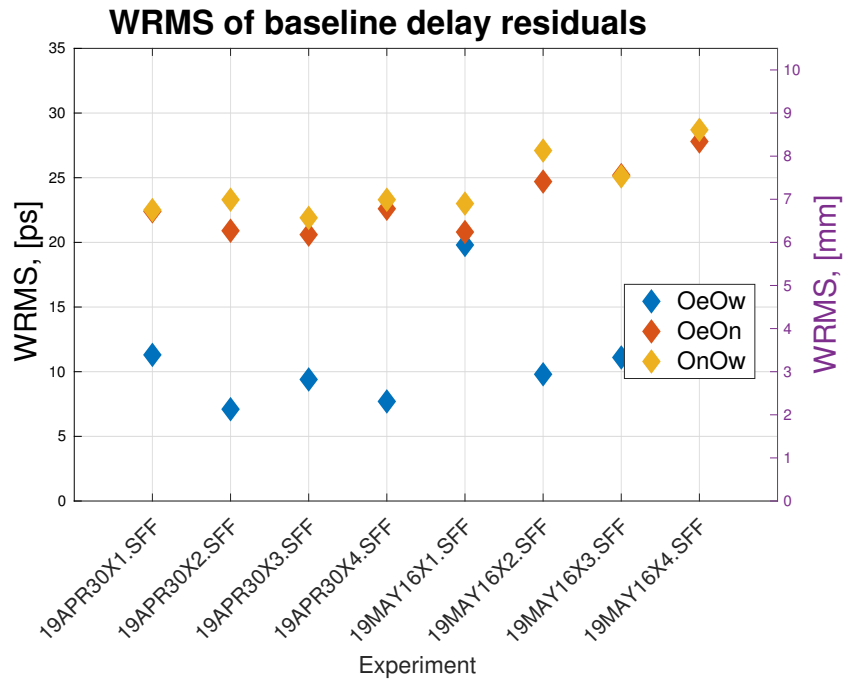


**Figure 4.8:** The WRMS of all experiments, with corrections made for air pressure

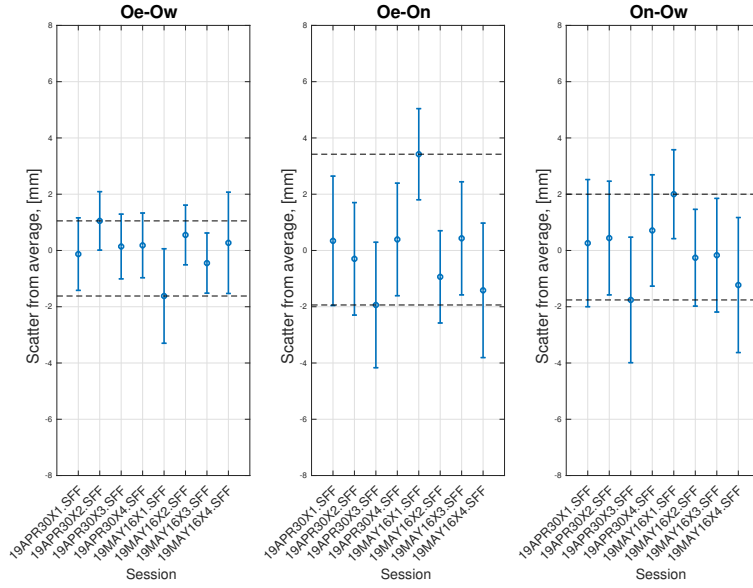


**Figure 4.9:** Plots of scatter around the average baseline length, calculated from all included sessions. Scatter in mm along the y-axis and session name on the x-axis. The dashed lines represent the maximum and minimum scatter, respectively.

**Table 4.3:** WRMS of baseline residuals for each evaluated session in mm, together with the baseline lengths in metres, with uncertainty in mm. With pressure correction in log files

Session	WRMS,  LW LX XW  [mm]			LW [m]	LX [m]	XW [m]
K19120 <sub>1</sub>	2.10	6.75	5.79	74.9614 ± 1.29	468.6819 ± 2.30	540.3116 ± 2.26
K19120 <sub>2</sub>	2.04	5.70	6.33	74.9602 ± 1.04	468.6826 ± 2.00	540.3114 ± 2.02
K19120 <sub>3</sub>	1.95	5.85	5.76	74.9611 ± 1.15	468.6842 ± 2.23	540.3136 ± 2.23
K19120 <sub>4</sub>	1.98	5.49	5.28	74.9611 ± 1.15	468.6819 ± 2.00	540.3111 ± 1.98
K19136 <sub>1</sub>	4.11	4.14	3.69	74.9629 ± 1.68	468.6788 ± 1.62	540.3098 ± 1.58
K19136 <sub>2</sub>	1.92	4.35	6.33	74.9607 ± 1.06	468.6832 ± 1.64	540.3121 ± 1.72
K19136 <sub>3</sub>	1.95	5.49	6.24	74.9617 ± 1.07	468.6818 ± 2.01	540.3120 ± 2.02
K19136 <sub>4</sub>	3.33	7.53	7.32	74.9610 ± 1.80	468.6837 ± 2.39	540.3131 ± 2.40
Weighted averages & sigmas:				74.9611 ± 0.15	468.6822 ± 0.62	540.3121 ± 0.46

In the above figures, it can be clearly seen that the result obtained on the baseline between the two twin telescopes both exhibit a smaller scatter about the average and a smaller uncertainty than the baseline measurement between the twin telescopes and the 20 metre telescope. The effects of correcting the tropospheric pressure in the log file is small, and seems to effect the result on the sub-millimetre level. Further experiments should investigate this more thoroughly.

## 4.4 Summary of results

This section is intended to summarize the results obtained from all valid experiments. The data sets are divided into shorter segments of up to six hours, and multiband

solutions are obtained from these. The two available 24 hour experiments are also used to obtain a multiband solution, as well as a phase solution.

#### 4.4.1 Shorter Data Segments and Multiband Solutions

The results presented here contain 11 datasets of up to six hours in length, performed using all three telescopes at the Onsala Space Observatory, performed in April and May of 2019. Table 4.4 below details the sessions used, how long each session lasts and how many scans were used per analysis.

**Table 4.4:** Details on the Experiments Used in this Analysis

Session	Duration [h]	# of scans	# of scans used
K19120 <sub>1</sub>	6	644	557 (86.49%)
K19120 <sub>2</sub>	6	635	570 (89.76%)
K19120 <sub>3</sub>	6	659	563 (85.43%)
K19120 <sub>4</sub>	6	648	543 (83.80%)
K19120 <sub>5</sub>	6	574	452 (78.75%)
K19135	4	574	471 (82.06%)
K19136 <sub>1</sub>	6	858	666 (77.62%)
K19136 <sub>2</sub>	6	822	650 (79.08%)
K19136 <sub>3</sub>	6	852	705 (82.75%)
K19136 <sub>4</sub>	6	815	690 (84.66%)
K19142	6	823	691 (83.96%)

Similar to Table 4.2 and Table 4.3 above, Table 4.5 below presents the results obtained through  $\nu$ Solve.

**Table 4.5:** WRMS of baseline residuals for each evaluated session in mm, together with the baseline lengths in metres, with uncertainty in mm. All available sessions, with pressure correction performed as outlined above.

Session	WRMS,  LW LX XW  [mm]			LW [m]	LX [m]	XW [m]
K19120 <sub>1</sub>	2.10	6.75	5.79	74.9614 $\pm$ 1.29	468.6819 $\pm$ 2.30	540.3116 $\pm$ 2.26
K19120 <sub>2</sub>	2.04	5.70	6.33	74.9602 $\pm$ 1.04	468.6826 $\pm$ 2.00	540.3114 $\pm$ 2.02
K19120 <sub>3</sub>	1.95	5.85	5.76	74.9611 $\pm$ 1.15	468.6842 $\pm$ 2.23	540.3136 $\pm$ 2.23
K19120 <sub>4</sub>	1.98	5.49	5.28	74.9611 $\pm$ 1.15	468.6819 $\pm$ 2.00	540.3111 $\pm$ 1.98
K19120 <sub>5</sub>	0.93	10.3	9.90	74.9613 $\pm$ 0.87	468.6834 $\pm$ 4.80	540.3127 $\pm$ 4.80
K19135	2.37	5.34	5.73	74.9602 $\pm$ 1.40	468.6811 $\pm$ 2.08	540.3097 $\pm$ 2.10
K19136 <sub>1</sub>	4.11	4.14	3.69	74.9629 $\pm$ 1.68	468.6788 $\pm$ 1.62	540.3109 $\pm$ 1.58
K19136 <sub>2</sub>	1.92	4.35	6.33	74.9607 $\pm$ 1.06	468.6832 $\pm$ 1.64	540.3121 $\pm$ 1.72
K19136 <sub>3</sub>	1.95	5.49	6.24	74.9617 $\pm$ 1.07	468.6818 $\pm$ 2.01	540.3120 $\pm$ 2.02
K19136 <sub>4</sub>	3.33	7.53	7.32	74.9610 $\pm$ 1.80	468.6837 $\pm$ 2.39	540.3131 $\pm$ 2.40
K19142	1.89	4.08	5.64	74.9618 $\pm$ 0.97	468.6820 $\pm$ 1.83	540.3122 $\pm$ 1.88
Weighted averages & sigmas:				74.9612 $\pm$ 0.19	468.6819 $\pm$ 0.48	540.3115 $\pm$ 0.36



## 4. Results

Comparing the results obtained with a multiband solution between shorter data sets and longer data sets, a slight but clear improvement is seen when increasing the amount of scans in the analysis. At the same time, using the phase observable rather than the multiband delay sees a slight increase in performance, particularly on the twin telescope baseline.

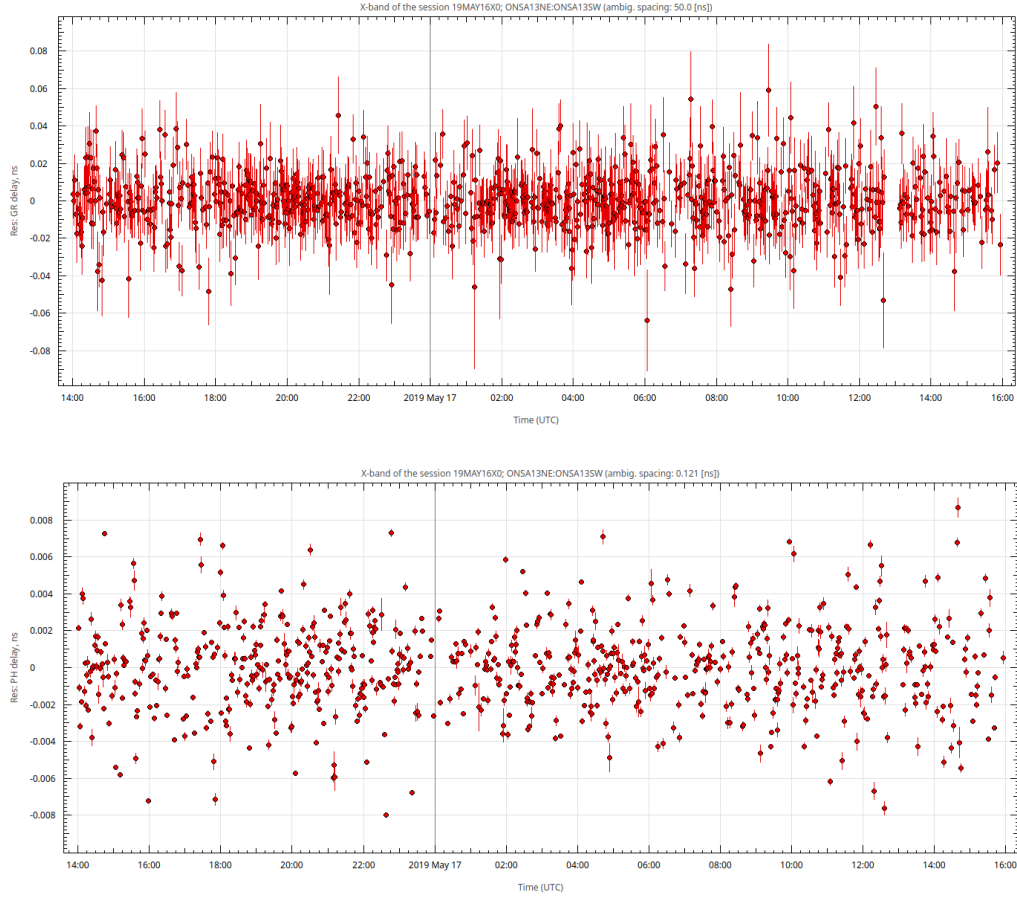


**Figure 4.11:** Comparison of delay residuals from Multiband (upper figure) and Phase (lower figure) evaluation. This figure shows the result on the OTT baseline. The scale of the Multiband residuals is  $\pm 0.1$  ns, while the scale of the Phase residuals is  $\pm 0.01$  ns



# 5

## Conclusion

### 5.1 Analysis and Discussion on the Results

The results themselves show an uncertainty similar to the one seen when using legacy VLBI systems, which indicate that the weakest link in these experiments is the 20 metre telescope, and by extension, the legacy VLBI systems as a whole when performing these local-tie measurements on other observatories with similar setups. The results obtained during the course of this work, however, lies within expected values, both as estimated by using Eq. (2.3a) and when comparing with a similar experiment carried out at the Wettzell observatory in 2014 and 2015 [8].

The discrepancy in the result on the twin telescope baseline compared to the baseline between the two twins and the 20 metre telescope may be due to different factors. One of the more likely culprits would be the mismatch in polarization between the telescopes, resulting in a loss in signal when the different telescopes are correlated. The newer systems installed on the twin telescopes may also perform better, although this difference is not quantified in the scope of this masters thesis. Comparing the SNR of the baselines, either by looking at fringe plots in *fourfit* or in *νSolve* reveals an on average slightly higher SNR on the baseline between the twin telescopes, which could be one of the reasons for this more accurate result.

The use of longer data sets offer an increase in accuracy, but not as much as Eq. (2.22) would suggest. In principle, a data set of 24 hours should on average contain four times the number of samples taken compared to a six hour experiment. Increasing the number of samples by a factor of four should decrease the uncertainty by roughly the same factor. Possible reasons for this could be lower than believed system stability, imperfect phase calibration over the course of 24 hours which may or may not be sufficient compared to a shorter time period, and possibly different amount of scans actually used in the different solutions.

#### 5.1.1 A note on the Omitted Frequency Channel

Since a frequency band was omitted from the analysis, it is of some importance to attempt to characterize its effect on the overall result. Calculating the RMS bandwidth from Eq. (2.3a) with the center frequencies used in the experiments and simply removing the first frequency channel yields a decrease in the spanned RMS bandwidth of about 6 %, Calculating Eq. (2.3b), assuming the amount of samples,  $N$ , are decreased by 1/8, since one of eight frequency channels are omitted, the total SNR decreases by about 7 % for a total increase in the uncertainty of roughly 12 %.

Further investigation into finding another channel to use should be performed, to be able to utilize the full 8 channels and the associated bandwidth.

### 5.2 Future Work

This thesis work has focused on the baselines between the new Onsala Twin Telescopes and the older 20 metre telescope. In principle, the knowledge gained from this work can be easily adapted to also include the 25 metre telescope, but at a different frequency range. In the case of the 25 metre telescope, this would be the *C* band.

Ideally, it would be preferable to also include the *S* band of both the OTTs and the 20 metre telescope, in order to have a larger synthesized bandwidth and smaller uncertainties in the measurements. Dual-frequency setups also allow for a more accurate removal of ionospheric effects. Even though a short baseline such as those found at OSO largely removes the effects of the ionosphere, even more accurate estimations can be made when observing at two or more frequencies. However, this approach would require extremely careful work in minimizing the effects of RFI, since these tend to be correlated on a short baseline, on the lower frequency bands, as has been shown in the multi-band analysis of the the twin telescopes.

Additionally, the baseline and WRMS derived from the phase observable could be improved in its accuracy by implementing a more robust manual phase calibration regime, or if possible to remove, utilize the pcal tones already in use in VLBI.

Alternatively, the legacy receiver of the 20 and 25 metre telescopes could be configured together with the OTTs to observe 14 channels in the *X*-band, each with 16 or 32 MHz of channel bandwidth, mitigating the RFI while still obtaining a large spanned bandwidth for even more accurate measurements.

# Bibliography

- [1] M Pantaleev et al. “Design, Implementation and Tests of the Signal Chain for the Twin Telescopes at Onsala Space Observatory”. In: *23rd European VLBI Group for Geodesy and Astrometry Working Meeting*. 2017, pp. 15–19.
- [2] RJ Sault and MH Wieringa. “Multi-frequency synthesis techniques in radio interferometric imaging.” In: *Astronomy and Astrophysics Supplement Series* 108 (1994), pp. 585–594.
- [3] UN-GGIM, ed. *UN-GGIM Global Geodetic Reference Frame Resolution*. United Nations Committee of Experts on Global Geospatial Information Management. Dec. 2014.
- [4] K Akiyama et al. “First M87 Event Horizon Telescope Results. II. Array and Instrumentation”. In: *The Astrophysical Journal Letters* 875.1 (2019), p. L2.
- [5] AR Thompson et al. *Interferometry and synthesis in radio astronomy*. Wiley New York et al., 1986.
- [6] H Schuh and D Behrend. “VLBI: a fascinating technique for geodesy and astrometry”. In: *Journal of Geodynamics* 61 (2012), pp. 68–80.
- [7] PJ Diamond JA Zensus and PJ Napier. “Geodetic Measurements with VLBI”. In: (1995).
- [8] T Schüler et al. “Initial results obtained with the first TWIN VLBI radio telescope at the Geodetic Observatory Wettzell”. In: *Sensors* 15.8 (2015), pp. 18767–18800.
- [9] A Niell et al. “Demonstration of a Broadband Very Long Baseline Interferometer System: A New Instrument for High-Precision Space Geodesy”. In: *Radio Science* 53.10 (2018), pp. 1269–1291.
- [10] PW Gorham. “Designing optimal bandwidth synthesis arrays for VLBI”. In: *The Telecommunications and Mission Operations Progress Report* 42 (1998), pp. 1–27.
- [11] JI Molinder. “A tutorial introduction to very long baseline interferometry (VLBI) using bandwidth synthesis”. In: *The Deep Space Network Progress Report* (1978), pp. 16–28.
- [12] Z Altamimi et al. “The terrestrial reference frame and the dynamic Earth”. In: *Eos, Transactions American Geophysical Union* 82.25 (2001), pp. 273–279.
- [13] C Ma et al. “The international celestial reference frame as realized by very long baseline interferometry”. In: *The Astronomical Journal* 116.1 (1998), p. 516.
- [14] AL Fey et al. “The second realization of the international celestial reference frame by very long baseline interferometry”. In: *The Astronomical Journal* 150.2 (2015), p. 58.

- [15] AT Deller et al. “DiFX: a software correlator for very long baseline interferometry using multiprocessor computing environments”. In: *Publications of the Astronomical Society of the Pacific* 119.853 (2007), p. 318.
- [16] R Capallo. *Visibility Amplitude Scaling: A Comparison of DiFX to the Mark4 Hardware Correlator*. 2011. URL: [https://www.haystack.mit.edu/tech/vlbi/hops/visibility\\_amplitude\\_scaling.pdf](https://www.haystack.mit.edu/tech/vlbi/hops/visibility_amplitude_scaling.pdf) (visited on 04/05/2019).
- [17] S Bolotin et al. “Transition to the vgosDb Format”. In: *9th IVS General Meeting*. 2016.
- [18] O Titov. “Least squares collocation method for space geodetic data analysis”. In: *Towards an Integrated Global Geodetic Observing System (IGGOS)*. Springer, 2000, pp. 238–240.
- [19] R Cappallo. “Delay and Phase Calibration in VGOS Post-Processing”. In: *International VLBI Service for Geodesy and Astrometry 2016 General Meeting Proceedings: "New Horizons with VGOS", Eds. Dirk Behrend, Karen D. Baver, Kyla L. Armstrong, NASA/CP-2016-219016, p. 61-64*. 2016, pp. 61–64.
- [20] KI Kellermann et al. “Very high-resolution observations of the radio sources NRAO 150, OJ 287, 3C 273, M87, 1633+ 38, BL Lacertae, and 3C 454.3”. In: *The Astrophysical Journal* 211 (1977), pp. 658–668.
- [21] H Berg. *Allgemeine Meteorologie: Einführung in die Physik der Atmosphäre*. Dümmler, 1948.

# A

## Appendix 1 - Example \*.vex and \*.v2d files

### A.1 Example \*.vex file

This is an example of a correctly configured \*.vex file necessary for the software correlator to work. The entries relating to individual scans and sources have been pruned to contain only one example of each.

```
VEX_rev = 1.5;
* sked version 2018Mar30
$GLOBAL;
  ref $EXPER = K19136;
  ref $SCHEDULING_PARAMS = SKED_PARAMS;
$EXPER;
  def K19136;
    exper_name = K19136;
    exper_description = "OSO X-band collocation session";
    PI_name = OSO;
    target_correlator = TBD;
  enddef;
*----- end $EXPER -----*
*----- begin $MODE -----*
$MODE;
  def VGEO-X8.XX;
    ref $FREQ = VGEO-X8-XX01:On;
    ref $FREQ = VGEO-X8-XX02-VDIF:Oe:Ow;
    ref $BBC = VGEO-X8-XX01:On;
    ref $BBC = VGEO-X8-XX02-VDIF:Oe:Ow;
    ref $IF = VGEO-X8-XX01:On;
    ref $IF = VGEO-X8-XX02:Oe:Ow;
    ref $TRACKS = Mk341_1f_2b-XX01:On:Oe:Ow;
    ref $HEAD_POS = Mk341-XX01S01:On:Oe:Ow;
    ref $PASS_ORDER = Mk341-XX01S01:On:Oe:Ow;
    ref $ROLL = NO_ROLL:On:Oe:Ow;
    ref $PHASE_CAL_DETECT = Standard:On:Oe:Ow;
    ref $TRACKS = Mark5B_format:On;
    ref $TRACKS = VDIF_format:Oe:Ow;
  enddef;
*----- end $MODE -----*
*----- begin $STATION -----*
$STATION;
  def On;
    ref $SITE = ONSALA60;
    ref $ANTENNA = ONSALA60;
    ref $DAS = DBBC_DDC_rack;
    ref $DAS = On_02;
    ref $DAS = FlexBuff_recorder;
    ref $DAS = thin_tape;
    ref $DAS = high_density;
  enddef;
  def Oe;
    ref $SITE = ONSA13NE;
    ref $ANTENNA = ONSA13NE;
    ref $DAS = DBBC_DDC_rack;
    ref $DAS = Oe_Oe;
    ref $DAS = FlexBuff_recorder;
    ref $DAS = thin_tape;
    ref $DAS = high_density;
  enddef;
  def Ow;
    ref $SITE = ONSA13SW;
    ref $ANTENNA = ONSA13SW;
    ref $DAS = DBBC_DDC_rack;
    ref $DAS = Ow_Ow;
    ref $DAS = FlexBuff_recorder;
    ref $DAS = thin_tape;
    ref $DAS = high_density;
  enddef;
```

## A. Appendix 1 - Example \*.vex and \*.v2d files

---

```

*----- end $STATION -----*
*----- begin $ANTENNA -----*
$ANTENNA;
  def ONSALA60;
    antenna_diam = 20.00 m;
    axis_type = az : el;
    axis_offset = 0.00000 m;
    antenna_motion = az : 183.0 deg/min : 20 sec;
    antenna_motion = el : 60.0 deg/min : 18 sec;
    pointing_sector = &n : az : 340.0 deg : 740.0 deg : el : 5.0 deg : 85.0 deg;
  enddef;
  def ONSA13NE;
    antenna_diam = 13.20 m;
    axis_type = az : el;
    axis_offset = 0.00000 m;
    antenna_motion = az : 720.0 deg/min : 0 sec;
    antenna_motion = el : 360.0 deg/min : 0 sec;
    pointing_sector = &n : az : 270.0 deg : 810.0 deg : el : 5.0 deg : 90.0 deg;
  enddef;
  def ONSA13SW;
    antenna_diam = 13.20 m;
    axis_type = az : el;
    axis_offset = 0.00000 m;
    antenna_motion = az : 720.0 deg/min : 0 sec;
    antenna_motion = el : 360.0 deg/min : 0 sec;
    pointing_sector = &n : az : 270.0 deg : 810.0 deg : el : 5.0 deg : 90.0 deg;
  enddef;
*----- end $ANTENNA -----*
*----- begin $BBC -----*
$BBC;
  def VGEO-X8-XX01;
    BBC_assign = &BBC01 : 01 : &IF_A1;
    BBC_assign = &BBC02 : 02 : &IF_A1;
    BBC_assign = &BBC03 : 03 : &IF_A1;
    BBC_assign = &BBC04 : 04 : &IF_A1;
    BBC_assign = &BBC05 : 05 : &IF_B1;
    BBC_assign = &BBC06 : 06 : &IF_B1;
    BBC_assign = &BBC07 : 07 : &IF_B1;
    BBC_assign = &BBC08 : 08 : &IF_B1;
  enddef;
  def VGEO-X8-XX02-VDIF;
    BBC_assign = &BBC01 : 01 : &IF_1N;
    BBC_assign = &BBC02 : 02 : &IF_1N;
    BBC_assign = &BBC03 : 03 : &IF_1N;
    BBC_assign = &BBC04 : 04 : &IF_1N;
    BBC_assign = &BBC05 : 05 : &IF_1N;
    BBC_assign = &BBC06 : 06 : &IF_1N;
    BBC_assign = &BBC07 : 07 : &IF_1N;
    BBC_assign = &BBC08 : 08 : &IF_1N;
    BBC_assign = &BBC09 : 09 : &IF_3N;
    BBC_assign = &BBC10 : 10 : &IF_3N;
    BBC_assign = &BBC11 : 11 : &IF_3N;
    BBC_assign = &BBC12 : 12 : &IF_3N;
    BBC_assign = &BBC13 : 13 : &IF_3N;
    BBC_assign = &BBC14 : 14 : &IF_3N;
    BBC_assign = &BBC15 : 15 : &IF_3N;
    BBC_assign = &BBC16 : 16 : &IF_3N;
  enddef;
*----- end $BBC -----*
*----- begin $DAS -----*
$DAS;
  def DBBC_DDC_rack;
    electronics_rack_type = DBBC_DDC;
  enddef;
  def Mark5B_recorder;
    record_transport_type = Mark5B;
  enddef;
  def FlexBuff_recorder;
    record_transport_type = FlexBuff;
  enddef;
  def On_02;
    recording_system_ID = 02;
  enddef;
  def Oe_Oe;
    recording_system_ID = Oe;
  enddef;
  def Ow_Ow;
    recording_system_ID = Ow;
  enddef;
  def 1_recorder;
    number_drives = 1;
  enddef;
  def 2_recorder;
    number_drives = 2;
  enddef;
  def low_density;
    record_density = 33333 bpi;
  enddef;
  def high_density;
    record_density = 56250 bpi;
  enddef;
  def thick_tape;
    tape_length = 8800 ft;
  enddef;
  def thin_tape;

```



## A. Appendix 1 - Example \*.vex and \*.v2d files

---

```
scan 136-1401;
*----- end $SCHED -----*
*----- begin $SITES -----*
$SITE;
def ONSALA60;
  site_type = fixed;
  site_name = ONSALA60;
  site_ID = On;
  site_position = 3370606.045 m : 711917.494 m : 5349830.726 m;
  occupation_code = 72137701;
enddef;
def ONSA13NE;
  site_type = fixed;
  site_name = ONSA13NE;
  site_ID = Oe;
  site_position = 3370889.190 m : 711570.780 m : 5349691.100 m;
  horizon_map_az = 0.0 deg : 8.0 : 215.0 : 226.0 : 240.0 : 252.0 : 315.0 : 360.0;
  horizon_map_el = 8.0 deg : 5.0 : 10.0 : 5.0 : 9.0 : 5.0 : 8.0 : 8.0;
  occupation_code = 00000000;
enddef;
def ONSA13SW;
  site_type = fixed;
  site_name = ONSA13SW;
  site_ID = Ow;
  site_position = 3370946.720 m : 711534.140 m : 5349659.940 m;
  occupation_code = 00000000;
enddef;
*----- end $SITES -----*
*----- begin $SOURCE -----*
$SOURCE;
def 0003-066;
  source_type = star;
  source_name = 0003-066;
  IAU_name = 0003-066;
  ra = 00h06m13.89289s;
  dec = -06d23'35.3353";
  ref_coord_frame = J2000;
enddef;
*----- end $SOURCE -----*
*----- begin $TRACKS -----*
$TRACKS;
def Mk341_1f_2b-XX01;
  fanout_def = A : &CH01 : sign : 1 : 02;
  fanout_def = A : &CH01 : mag : 1 : 03;
  fanout_def = A : &CH02 : sign : 1 : 04;
  fanout_def = A : &CH02 : mag : 1 : 05;
  fanout_def = A : &CH03 : sign : 1 : 06;
  fanout_def = A : &CH03 : mag : 1 : 07;
  fanout_def = A : &CH04 : sign : 1 : 08;
  fanout_def = A : &CH04 : mag : 1 : 09;
  fanout_def = A : &CH05 : sign : 1 : 10;
  fanout_def = A : &CH05 : mag : 1 : 11;
  fanout_def = A : &CH06 : sign : 1 : 12;
  fanout_def = A : &CH06 : mag : 1 : 13;
  fanout_def = A : &CH07 : sign : 1 : 14;
  fanout_def = A : &CH07 : mag : 1 : 15;
  fanout_def = A : &CH08 : sign : 1 : 16;
  fanout_def = A : &CH08 : mag : 1 : 17;
enddef;
def Mark4_format;
  track_frame_format = Mark4;
enddef;
def Mark5B_format;
  track_frame_format=VDIF;
enddef;
def VDIF_format;
  track_frame_format = VDIF;
enddef;
*----- end $TRACKS -----*
*----- begin $CLOCK -----*
$CLOCK;
def Oe; clock_early = 2019y136d12h00m : -27.712431 usec : 2019y138d12h00m0s : -0.450e-12; enddef;
def Ow; clock_early = 2019y136d12h00m : -27.856174 usec : 2019y138d12h00m0s : -0.450e-12; enddef;
def On; clock_early = 2019y136d12h00m : -32.73134832636966 usec : 2019y138d12h00m0s : 0.0; enddef;
*----- end $CLOCK -----*
*----- begin $EOP -----*
$EOP;
def EOP134;
  TAI-UTC= 37 sec;
  A1-TAI= 0 sec;
  eop_ref_epoch=2019y134d;
  num_eop_points=1;
  eop_interval=24 hr;
  ut1-utc = -0.019559 sec;
  x_wobble = 0.06715 asec;
  y_wobble = 0.40964 asec;
enddef;
def EOP135;
  TAI-UTC= 37 sec;
  A1-TAI= 0 sec;
  eop_ref_epoch=2019y135d;
  num_eop_points=1;
  eop_interval=24 hr;
  ut1-utc = -0.020021 sec;
  x_wobble = 0.06863 asec;
```



```

    y_wobble = 0.41012 asec;
enddef;
def EOP136;
    TAI-UTC= 37 sec;
    A1-TAI= 0 sec;
    eop_ref_epoch=2019y136d;
    num_eop_points=1;
    eop_interval=24 hr;
    ut1-utc = -0.020522 sec;
    x_wobble = 0.07030 asec;
    y_wobble = 0.41076 asec;
enddef;
def EOP137;
    TAI-UTC= 37 sec;
    A1-TAI= 0 sec;
    eop_ref_epoch=2019y137d;
    num_eop_points=1;
    eop_interval=24 hr;
    ut1-utc = -0.020021 sec;
    x_wobble = 0.07224 asec;
    y_wobble = 0.41147 asec;
enddef;
def EOP138;
    TAI-UTC= 37 sec;
    A1-TAI= 0 sec;
    eop_ref_epoch=2019y138d;
    num_eop_points=1;
    eop_interval=24 hr;
    ut1-utc = -0.021663 sec;
    x_wobble = 0.07418 asec;
    y_wobble = 0.41222 asec;
enddef;
*----- end $EOP -----*
```

## A.2 Example \*.v2d file

This is an example of a properly configured \*.v2d file. Of particular note are the lines detailing the format used to record the data, which needs to be carefully defined in order for the correlator to handle the raw data. Also of importance is the use of the built in frequency band "zoom" function, even though in this particular example, all three telescopes record at a 32 MHz bandwidth. If the zoom function is not used when combining upper and lower sideband recordings, as is the case with these experiments, the correlator will not function properly.

```

maxLength = 172800
singleSetup = false
singleScan = false
nCore=12 nThread=12

tweakIntTime = true

SETUP setup
{
    strideLength=0
    xmacLength=0
    tInt=1
    specRes=0.5
    FFTSpecRes=0.25
    doPolar=true
    guardNS=2000
}

antennas = Oe,Ow,On

vex = k19136.vex

ANTENNA Oe
{
    fileList=oe.files
    format = VDIF_16416-2048-16-2
    sampling = REAL
    zoom = zoom2
    phaseCalInt = 5
}

ANTENNA Ow
{
    fileList=ow.files
    format = VDIF_16416-2048-16-2
    sampling = REAL
```

## A. Appendix 1 - Example \*.vex and \*.v2d files

---

```
        zoom = zoom2
        phaseCalInt = 0
    }
ANTENNA On
{
    filelist=on.files
    sampling = REAL
    format = VDIF_8032-1024-8-2
    zoom = zoom2
    phaseCalInt = 1
}
ZOOM zoom2
{
    addZoomFreq = freq@8212.99/bw@32.0/noparent@true
    addZoomFreq = freq@8252.99/bw@32.0/noparent@true
    addZoomFreq = freq@8352.99/bw@32.0/noparent@true
    addZoomFreq = freq@8512.99/bw@32.0/noparent@true
    addZoomFreq = freq@8732.99/bw@32.0/noparent@true
    addZoomFreq = freq@8852.99/bw@32.0/noparent@true
    addZoomFreq = freq@8892.99/bw@32.0/noparent@true
    addZoomFreq = freq@8932.99/bw@32.0/noparent@true
}
```

# B

## Appendix 2 - Scripts

Provided here are a couple of helper scripts that should make the editing of configure files and post-correlation operations a little easier.

### B.1 fieldReplacer

```
#!/bin/sh
#!/usr/bin/sh

case $1 in
  "-help"|" -h"|" --h"|" --help")
    echo "This script allows for the replacement of vex file blocks."
    echo "Calling for the script using [-h, --h, -help, --help] displays this text and closes the program."
    echo "Normal use: bash fieldReplacer <origin file> <field> <target file>."
    echo "The origin file should be a known properly configured vex file in terms of data fields consisting of begin and end fields."
    echo "The script will scrape the selected field from the origin file and replace the corresponding field in the target file."
    echo "Valid fields can be found by running this script with: bash fieldReplacer <origin file> [-valids] without the field argument."
    exit 1
    ;;
  "-valids")
    echo "hello"
    grep -n "begin" $2
    echo "Exiting."
    exit 1
    ;;
  *)
    esac

file=$1
field=$2
file2=$3
rm -f inter2 test
echo $file
echo $field
echo $file2
grep -n "begin \\\${field}" $file > inter
grep -n "end \\\${field}" $file >> inter

awk -F': ' '{print $1}' inter > inter2
let i=0
declare -a vals
while IFS=$'\n' read -r line; do
  #echo $line
  echo $i
  vals[i]=$line
  echo ${vals[i]}

  let i=i+1
done < inter2
echo ${vals[0]}
echo ${vals[1]}
declare -i a=${vals[0]}
declare -i b=${vals[1]}
echo $a $b
sed -n "${a},${b}p" $file > $field.file
cp $field.file temp
grep -n "begin \\\${field}" $file2 > interRep
grep -n "end \\\${field}" $file2 >> interRep
awk -F': ' '{print $1}' interRep > interRep2

let j=0
declare -a valsRep
while IFS=$'\n' read -r line; do
  #echo $line
  echo $j
  valsRep[j]=$line
  echo ${valsRep[j]}
```

```
let j=j+1
done < interRep2

declare -i a=${valsRep[0]}
declare -i b=${valsRep[1]}
declare -i c=${a-1}
echo $c
echo $a $b
sed -i "${a},${b}d" $file2
sed -i "${c}"rtemp $file2

rm inter inter2 interRep interRep2 temp
```

### B.2 vex2refsource

This simple script allows the operator to view the fringe-plots of a specific source, baseline and polarization after correlation has been performed and conversion to the mk4 format has been performed. This is useful, when for instance, finding good scans of a particular strong source to do manual phase calibration with. It uses the \*.vex file pertaining to a particular experiment as an input, together with a control file. The only inputs needed are the three first: The \*.vex file, the source and the experiment name.

```
#!/bin/bash
#!/usr/bin/sh

file=$1 #Vex file
source=$2 #Source scans to be analyzed, for example NRAO150
exp=$3 #Directory of mk4 files
baseline=$4 #Which baseline to analyze.
polarization=$5 #Which polarization to analyze
cfile=$6 #which control file to use

grep -B 3 "source = $source" $file > scans
awk -F' ' '/scan/ {print $2}' scans > scans2
sed -i 's/.$//' scans2

declare -a scan
let i=0
while IFS=$'\n' read -r line; do
#echo $i
scan[$i]=$line
read -n 1 -p "Press any key to continue, ctrl+c to exit" < /dev/tty | fourfit -pt -b $baseline -P "$polarization"
-c $cfile $e$
let i=i+1
done < scans2

rm scans scans2
```